Multi-dimensional wavelet reduction for the homogenisation of microstructures

Available online at www.sciencedirect.com
ScienceDirect
Comput. Methods Appl. Mech. Engrg. 359 (2020) 112652
Computer methods in applied mechanics and engineering
www.elsevier.com/locate/cma

Multi-dimensional wavelet reduction for the homogenisation of microstructures

Rody A. van Tuijl, Joris J.C. Remmers*, Marc G.D. Geers

Eindhoven University of Technology, P.O. Box 513, Eindhoven, The Netherlands

Received 25 April 2019; received in revised form 26 August 2019; accepted 22 September 2019
Available online 5 November 2019

Abstract

One of the recent fields of interest in computational homogenisation is the development of model order reduction frameworks to address the significant computational costs enabling fast and accurate evaluation of the microstructural volume element. Model order reduction techniques are applied to computationally challenging analyses of detailed micro- and or macro-structural problems to reduce both computational time and memory usage. In order to alleviate the costly integration, a wavelet-reduced order model for one-dimensional microstructural problems was presented in van Tuijl et al. (2019). This novel approach addresses both the large number of degrees of freedom and integration costs and provides control on errors in the microstructural fields. In this work, this wavelet reduced order model is extended to a multi-dimensional framework and benchmarked for more realistic multi-scale problems.

The Wavelet-Reduced Order Model consists of two reduction steps. First, a Reduced Order Model is constructed to reduce the dimensionality of the microstructural model. Second, a wavelet representation is applied to reduce the integration costs of the microstructural model, whilst maintaining control over the local integration error. The multi-dimensional Wavelet-Reduced Order Model is demonstrated for a set of two-dimensional path-dependent microstructural models, evaluating their accuracy and reduction with respect to the full order models on the microstructural and homogenised fields.

MSC: 00-01; 99-00

Keywords: Model reduction; Wavelets; Multi-dimensionality; Numerical integration; Micro-mechanics

1. Introduction

Computational Homogenisation (CH) is an accurate numerical technique to directly derive the macro-scale material properties from the underlying microstructure [1]. In this framework, the microstructure of the material is modelled explicitly by means of a *representative volume element* (RVE). In case the RVE shows linear behaviour, the macro-scale properties in terms of the tangent stiffness can be obtained directly through static condensation of the stiffness matrix of the RVE. When applying this technique to a micro-structure that shows a non-linear material behaviour, repetitive solving of the microstructural *Partial Differential Equation* (PDE) is required [2]. Apart from the additional computational costs, the amount of data increases as well. For history-dependent material models,

* Corresponding author.
E-mail addresses: r.a.v.tuijl@tue.nl (R.A. van Tuijl), j.j.c.remmers@tue.nl (J.J.C. Remmers), m.g.d.geers@tue.nl (M.G.D. Geers).

https://doi.org/10.1016/j.cma.2019.112652

the state of all microstructural material points and history parameters need to be stored. The storage needed for the history parameters in addition to the computational time required to solve all the microstructural models imposes severe restrictions on the maximum feasible number of degrees of freedom used at the macro-scale as well as the micro-scale [3]. The CH framework would therefore greatly benefit from a reduced order modelling approach.

Reducing the computational efforts is often achieved by the extraction of a reduced set of global basis functions using the *Proper Orthogonal Decomposition* (POD) forming a *Reduced Order Model* (ROM), as shown by Yvonnet and He [4], among many others. As pointed out by Rathinam and Petzold [5], the computational costs do not scale proportionally with the reduction of number of degrees of freedom when non-linear microstructural models are considered, as the integration of the internal forces and stiffness tensors requires a full integration of the fields.

For this reason, a second reduction step can be introduced to reduce the computational costs involved with the integration of the microstructural fields. Methods employing this two-step reduction technique are often referred to as *hyper-reduction* methods, a term coined by Ryckelynck [6]. A key element of these methods is the reduction of the computational costs of the numerical integration procedure required to assemble the system of equations.

In hyper-reduction methods, not only the dimensionality of the problem but also the integration costs and storage of history variables are reduced. This second reduction is achieved via an approximation of the integral. Hyper-reduction methods can be roughly divided into two classes. The first class contains the *empirical interpolation methods* (EIM) [7], which apply a least-square fitting of a modal representation of the integrand at a pre-selected subset of integration points. Notable implementations of this approach are: *High-Performance-Reduced Order Modelling* (HP-ROM) [8], *Discrete Empirical Interpolation Method* (DEIM) [9], *Missing Point Estimation* (MPE) [10]. The second class, often denoted as reduced quadrature schemes, are constructed from a subset of integration points with weights assigned that minimise the integration error for the snapshots as shown by An et al. [11], e.g. *Empirical Cubature Method* (ECM) [12], *Energy-Conserving Sampling and Weighting hyper reduction* (ECSW) [13]. A detailed comparison of the two classes is presented in [3].

Alternatively, Dvorak and Benveniste [14] proposed the *Transformation Field Analysis* technique (TFA) to reduce the computational costs of microstructural models. The latter is achieved by a piecewise constant approximation of the strain field and internal variables, thereby reducing the number of degrees of freedom and the costs entailed with integration and assembly of the system of equations. A nonuniform approximation of the internal variables was presented by Michel and Suquet [15], yielding the *Nonuniform Transformation Field Analysis* (NTFA), which was extended to microstructures with elastic–viscoplastic constituents by Roussette et al. [16] and later to the *potential-based Reduced Basis Model Order Reduction* (pRBMOR) [17].

When the strain field is considered as a spatially varying signal comprising of different frequency components [18], it can also be compressed using sparse wavelet representations. An example utilising interpolating wavelet families to compress computationally challenging *initial-value problems* (IVP) is the predictor–corrector algorithm presented by Harnish et al. [19]. The IVP is solved on an adaptive grid resulting directly from the wavelet discretisation. In [20], this technique is used to construct a sparse wavelet representation of the internal force and stiffness integrands, yielding a computational efficient scheme to evaluate and integrate the ROM, albeit for one-dimensional models.

The multi-resolution nature of wavelets can be exploited to homogenise multi-resolution *partial differential equations* (PDE). The original idea of wavelet based numerical homogenisation was proposed by Beylkin and Brewster [21]. Andersson et al. [22] homogenised a PDE using a Haar wavelet filter. A two-dimensional multi-resolution homogenisation is shown by Dorobantu and Enquist [23]. Chertock and Levy improved the homogenisation scheme by approximating the high-frequency components and adding a fine-scale correction [24]. Later, Floréz et al. [25] employed a wavelet filter in combination with a regularised Petrov–Galerkin Gauss–Newton algorithm to reduce the dimensionality of the problem. Despite the reduction in dimensionality using wavelet filtering, the high-frequency (microstructural) reduction cannot be performed *a-priori* for non-linear problems. The computational costs in terms of CPU time and required memory involved with the solution of non-linear problems remain coupled to the spatial accuracy of the employed discretisation in contrary to ROM.

The aforementioned hyper-reduction methods relies on an *a-priori* reduction of the computational integration process. It is shown in [3] that the hyper-reduction of path-dependent models requires a high-dimensional snapshot space of the integrands. To relieve the requirements on the snapshot space a wavelet approximation of the integrals is proposed, leading to a one-dimensional *Wavelet-Reduced Order Model* (W-ROM) in [20].

The W-ROM entails a reduced basis and an adaptive wavelet approximation to control the error introduced in the reduction of the integrands during the evaluation of the model. The model omits the empirical selection of a reduced set of integration points by adaptively selecting integration points using a tolerance on the integrand. The W-ROM has demonstrated a reduction of both computational costs and memory usage for a one-dimensional non-linear microstructural problem by constructing a reduced grid to approximate the integrals present in ROM [20].

In this work, the one-dimensional W-ROM is extended to multiple dimensions to reduce the computational costs involved in the integration of the non-linear force terms occurring in multi-dimensional microstructural models. In addition to the extension of the W-ROM [20] to multi-dimensional micro-structures, this paper also focusses on the performance of the W-ROM scheme. The reduction level versus the integration and homogenisation accuracy of multi-dimensional micro-structures is evaluated for two multi-dimensional microstructural problems. The resulting reduction and the associated error will be compared to the original Finite Element discretised *Full Order Model* (FOM).

The paper is outlined as follows. In Section 2 the extension of the one-dimensional W-ROM model to the multi-dimensional setting is presented. A brief summary of the required multi-dimensional wavelet transforms and an outline of the applied integration techniques are given. For a more detailed explanation of wavelet approximations and the W-ROM framework the reader is referred to [26] and [20] respectively. Section 3 demonstrates the W-ROM of two microstructural problems. The conclusions and recommendations are presented in Section 4.

1.1. Notation

In this work, consistent notations are adopted. Using Einstein's notation convention, a Cartesian coordinate system with a set unit-length basis vectors $\vec{e}_i$ for $i = 1, \dots, D$, vectors are denoted by $\vec{a} = a_i \vec{e}_i$ and second order-tensors are denoted by $\mathbb{A} = A_{ij} \vec{e}_i \vec{e}_j$. For tensors of higher order (> 2), the order of the tensor is indicated by a pre-pended superscript, e.g. ${}^4\mathbb{C}$. Spaces and domains are indicated using calligraphic typesetting, e.g. $\mathcal{V}$.

A dyadic product between two vectors or tensors is denoted using $\vec{a} \otimes \vec{b} = {}^2\mathbb{C}$ or in index notation $a_i \vec{e}_i \otimes b_j \vec{e}_j = C_{ij} \vec{e}_i \vec{e}_j$.

Single and double contractions between tensors and vectors are denoted by $\cdot$ and $:$ respectively. In index notation, the contractions between tensors $\mathbb{A}$ and $\mathbb{B}$, $\mathbb{A} \cdot \mathbb{B}$ and $\mathbb{A} : \mathbb{B}$ evaluate to $A_{ik}B_{kj} \vec{e}_i \vec{e}_j$ and $A_{ij}B_{ji}$ respectively.

Normal and symmetric gradient are indicated using $\vec{\nabla}$ and $\vec{\nabla}^{\mathrm{s}}$, where $\vec{\nabla} = \partial_{x_i} \vec{e}_i$ and $\vec{\nabla}^{\mathrm{s}} \vec{a} = \frac{1}{2}[\vec{\nabla} \vec{a} + (\vec{\nabla} \vec{a})^{\mathrm{T}}]$. When a gradient operator is contracted with a vector or tensor, it denotes the divergence operator, e.g. $\vec{\nabla} \cdot \vec{a}$.

Column vectors and matrices are denoted by a single and double underline respectively, e.g. $\underline{v}$ and $\underline{\underline{M}}$.

2. Wavelet reduced order models

In this section the considered small-strain microstructural model and its coupling to the macro-scale are outlined first. Next, the two-step POD and wavelet based reduction of the microstructural model are described. Special attention is given to the approximation and integration of the internal forces and microstructural stresses.

2.1. Multi-scale problem description

The macro-structural problem (a) and underlying microstructural problems (b) of the homogenisation procedure are schematically depicted in Fig. 1. Here, $\mathcal{V}$ and $\partial\mathcal{V}$ are the microstructural domain and its boundary respectively. Note that the domain $\mathcal{V}$ might include voids. In this case, the boundaries of the voids on the edge of the microstructural problem are considered internal boundaries and are therefore not part of $\partial\mathcal{V}$. The microstructural stress and strain field are denoted by $\boldsymbol{\sigma}$ and $\boldsymbol{\varepsilon}$ respectively. The nonlinear constitutive stress–strain relation $\boldsymbol{\sigma} = \boldsymbol{\sigma}(\boldsymbol{\varepsilon}, \underline{\xi})$ used in this work depends on a set of history variables $\underline{\xi}$, which store the state of the material. For both the macro- and microstructural problems a small-strain description is employed. The volume of the micro-structure is denoted by $|\mathcal{V}|$. As this paper focusses on the solution of the microscale problem, variables without any subscript are defined in this domain. Variables in the macroscopic domain are denoted by a subscript M.

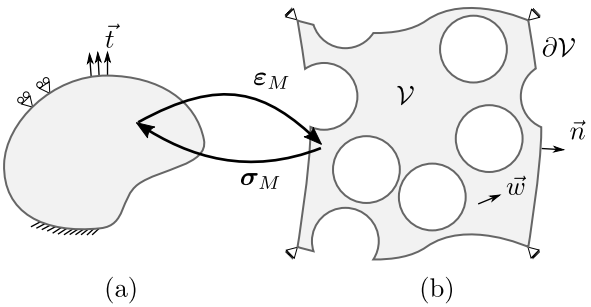

Fig. 1. Schematic outline of the computational homogenisation procedure, where (a) depicts the macroscopic problem and (b) depicts the microstructural problem with periodic boundary conditions.

2.2. Macro- and micro-scale coupling

The volume average of the microscopic strain is defined to be equal to the applied macroscopic strain $\boldsymbol{\varepsilon}_M = \frac{1}{|\mathcal{V}|}\int_{\mathcal{V}} \boldsymbol{\varepsilon}\,\mathrm{d}\mathcal{V}$ in its variational form. The homogenised macroscopic stress $\boldsymbol{\sigma}_M$ is defined as the volume averaged stress in the micro-structure:

$$\boldsymbol{\sigma}_M = \frac{1}{|\mathcal{V}|}\int_{\mathcal{V}} \boldsymbol{\sigma}\,\mathrm{d}\mathcal{V} \tag{1}$$

In accordance with the Hill–Mandel criterion [27], the micro-structure is subjected to the macro-scale strain $\boldsymbol{\varepsilon}_M$. Additionally, at the micro-scale strains will emerge from the micro-fluctuation field $\vec{w}(\vec{x})$, on which *Periodic Boundary Conditions* (PBC) are imposed to satisfy the condition on the volume averaged strain in its variational form, i.e. $\int_{\partial\mathcal{V}} \vec{w}\cdot\boldsymbol{\sigma}\cdot\vec{n}\,\mathrm{d}\partial\mathcal{V} = 0$. Note that a perfect interface is assumed.

2.3. Micro-structural model

In absence of body forces and assuming a small strain ansatz, the strong form of the linear momentum balance in the microstructural problem is given by (S):

$$\text{(S)}\begin{cases} \vec{\nabla}\cdot\boldsymbol{\sigma}(\boldsymbol{\varepsilon},\underset{\sim}{\xi}) = \vec{0} & \text{on } \mathcal{V} \\ \boldsymbol{\varepsilon}(\vec{x}) = \boldsymbol{\varepsilon}_M + \vec{\nabla}^{\mathrm{s}}\vec{w}(\vec{x}) & \text{on } \mathcal{V} \\ \vec{w}(\vec{x}) & \text{PBC on } \partial\mathcal{V} \end{cases} \tag{2}$$

After multiplication with a weighting function $\vec{q}(\vec{x})$ and integration over the microstructural domain, the Gauss divergence theorem is applied, giving the weak-form (W) of the microstructural problem: Find $\vec{w}\in\mathcal{W}$, such that

$$\text{(W)}\begin{cases} \int_{\partial\mathcal{V}} \vec{q}(\vec{x})\cdot\vec{t}(\vec{x})\,\mathrm{d}\partial\mathcal{V} - \int_{\mathcal{V}} \vec{\nabla}^{\mathrm{s}}\vec{q}(\vec{x}) : \boldsymbol{\sigma}(\boldsymbol{\varepsilon},\underset{\sim}{\xi})\,\mathrm{d}\mathcal{V} = \vec{0} & \text{for all } \vec{q}(\vec{x})\in\mathcal{Q} \\ \boldsymbol{\varepsilon}(\vec{x}) = \boldsymbol{\varepsilon}_M + \vec{\nabla}^{\mathrm{s}}\vec{w}(\vec{x}) & \text{on } \mathcal{V} \\ \vec{w}(\vec{x}) & \text{PBC on } \partial\mathcal{V} \end{cases} \tag{3}$$

where $\mathcal{Q} = \{\vec{q} \mid \vec{q}\in\mathcal{H}^1_0(\mathcal{V})\}$ and $\mathcal{W} = \{\vec{w} \mid \vec{w}\in\mathcal{H}^1(\mathcal{V})$ and $\vec{w}$ is periodic on $\partial\mathcal{V}\}$.

The traction on the boundary $\vec{t}$ is defined by $\vec{t} = \boldsymbol{\sigma}\cdot\vec{n}$ where $\vec{n}$ is the unit-length outward pointing normal vector on the boundary $\partial\mathcal{V} = \partial\mathcal{V}^+ \bigcup \partial\mathcal{V}^-$, where $\partial\mathcal{V}^+$ and $\partial\mathcal{V}^-$ are the opposing periodic boundary segments. The PBC require a force equilibrium between tractions $\vec{t}^{\,+}$ and $\vec{t}^{\,-}$ on their respective boundary segments $\partial\mathcal{V}^+$ and $\partial\mathcal{V}^-$, results in $\int_{\partial\mathcal{V}} \vec{q}\cdot\vec{t}\,\mathrm{d}\partial\mathcal{V} = 0$ since $\vec{t}^{\,+} = -\vec{t}^{\,-}$.

To discretise the FE problem, the weighting and trial functions are approximated using their discretised equivalents $\vec{q}(\vec{x}) \approx \vec{q}^{\,\mathrm{h}}(\vec{x})$ and $\vec{w}(\vec{x}) \approx \vec{w}^{\mathrm{h}}(\vec{x})$, where $\vec{q}^{\,\mathrm{h}}(\vec{x}) = \sum_i q_i\vec{N}_i(\vec{x})$ and $\vec{w}^{\mathrm{h}}(\vec{x}) = \sum_j w_j\vec{N}_j(\vec{x})$, using a set of Lagrangian basis functions $\vec{N}_k(\vec{x})$, where $k = 1, 2, \ldots, n^{\mathrm{d}}$ and n^{d} is the number of degrees of freedom in the employed finite element discretisation $\mathcal{V}^{\mathrm{h}}$ of the microstructural domain $\mathcal{V}$. The discretisation of the boundary $\partial\mathcal{V}$ is denoted by $\partial\mathcal{V}^{\mathrm{h}}$. Substitution of the discretised functions into the weak form (W) gives the

following discretised momentum balance (D):

$$\text{(D)} \begin{cases} \int_{\mathcal{V}^\text{h}} \vec{\nabla}^\text{s} \vec{N}_i(\vec{x}) : \boldsymbol{\sigma}(\boldsymbol{\varepsilon}, \vec{\xi})\, \mathrm{d}\mathcal{V}^\text{h} = 0 & \text{on } \mathcal{V}^\text{h} \\ \boldsymbol{\varepsilon}(\vec{x}) = \boldsymbol{\varepsilon}_M + \sum_j w_j \vec{\nabla}^\text{s} \vec{N}_j(\vec{x}) & \text{on } \mathcal{V}^\text{h} \end{cases} \tag{4}$$

The FE discretised system of equations (D) is solved in a standard fashion by applying Gaussian quadrature and using the Newton–Raphson method.

2.4. Dimensionality reduction

The dimensionality of the problem is reduced by considering a subspace of the complete FE solution space as a global basis for the ROM as shown in e.g. [4,8,20]. This reduced basis is found by storing a total of n^s snapshots of the micro-fluctuation $\vec{w}^\text{h}(\vec{x})$ obtained through different macroscopic loading paths $\boldsymbol{\varepsilon}_M = \boldsymbol{\varepsilon}_M(t)$. The resulting microfluctuation coefficients $\underline{w}$ are stored in a snapshot matrix $\underline{\underline{X}}$. A reduced basis, consisting of orthogonal micro-fluctuation modes $\underline{v}_i$ for $i = 1, \ldots, n^\text{m}$, is obtained using the *Proper Orthogonal Decomposition* of the snapshot matrix $\underline{\underline{X}}$. The singular values λ_i corresponding to mode $\underline{v}_i(\vec{x})$ represent the kinematic contribution to the micro-fluctuation fields encountered in the snapshots. The number of modes n^m is chosen such that the first n^m modes constitute the $1 - \delta^\text{rom}$ fraction of the cumulative sum of the singular values [28], where δ^rom is a predetermined ROM tolerance. The remaining modes are truncated. This can be written as follows:

$$\frac{\sum_{i=1}^{n^\text{m}} \lambda_i^2}{\sum_{i=1}^{n^\text{s}} \lambda_i^2} \geq 1 - \delta^\text{rom}$$

Using the coefficients v_{ik} resulting from the POD, the following (global) reduced basis functions $\vec{R}_j(\vec{x}) = \sum_k v_{jk} \vec{N}_k(\vec{x})$ for the microstructural problem are constructed from the original (local) finite element basis $\vec{N}_k(\vec{x})$ with $k = 1, 2, \ldots, n^\text{d}$ leading to the following reduced weighting function $\vec{Q}^\text{h}(\vec{x}) = \sum_i Q_i \vec{R}_i(\vec{x})$ and trial functions $\vec{W}^\text{h}(\vec{x}) = \sum_j W_j \vec{R}_j(\vec{x})$. Substitution of the reduced weighting and trial functions into the weak form (3) yields the ROM (R):

$$\text{(R)} \begin{cases} Q_i \int_{\mathcal{V}} \underbrace{\vec{\nabla}^\text{s} \vec{R}_i(\vec{x})}_{\boldsymbol{M}_i(\vec{x})} : \boldsymbol{\sigma}(\boldsymbol{\varepsilon}, \vec{\xi})\, \mathrm{d}\mathcal{V} = 0 & \text{for all } Q_i \\ \boldsymbol{\varepsilon}(\vec{x}) = \boldsymbol{\varepsilon}_M + \sum_j W_j \underbrace{\vec{\nabla}^\text{s} \vec{R}_j(\vec{x})}_{\boldsymbol{M}_j(\vec{x})} & \text{on } \mathcal{V}^\text{h} \end{cases} \tag{5}$$

where $\underline{\boldsymbol{M}}(\vec{x}) = \vec{\nabla}^\text{s} \underline{\vec{R}}(\vec{x})$ are the modal strain contributions. Note that the periodic boundary conditions are automatically satisfied, as the reduced bases $\vec{Q}^\text{h}(\vec{x})$ and $\vec{W}^\text{h}(\vec{x})$ are constructed using snapshots of the periodic fluctuation field $\vec{w}^\text{h}(\vec{x})$.

2.5. Reduction of the integration and storage costs

When solving the reduced problem (R) using Gaussian quadrature to perform the integration over the domain $\mathcal{V}$, a classical ROM is retrieved. As indicated by Rathinam and Petzold [5], the computational savings of non-linear ROM do not scale proportionally to the reduction in degrees of freedom. Although the computational costs for solving the algebraic system are reduced (by reducing the number of equations from n^d to n^m, where $n^\text{m} \ll n^\text{d}$), the assembly costs of the stiffness matrix and force vectors remain unaffected. Hyper-reduction methods, such as HP-ROM [8], ECM [12], ECSW [13] among many others, reduce the costs by interpolating (a part of) the integrand using a modal decomposition and a least-squares fitting onto pre-selected sample points or on the other hand using a subset of weighted Gauss points to approximate the integrand. The latter class of methods rely on a greedy selection of the integration points in the offline phase, during which the reduced model is constructed. A significant drawback of this approach is that there is no control on the local errors made during the online solution of the hyper-reduced model.

The *Wavelet-Reduced Order Model*, introduced in [20], employs a reduced integration procedure to include control on the local integration errors. The strains, stresses, history parameters and integrands of the internal force are approximated on a sparse dyadic grid using wavelets. The wavelet approximation of all required fields leads to

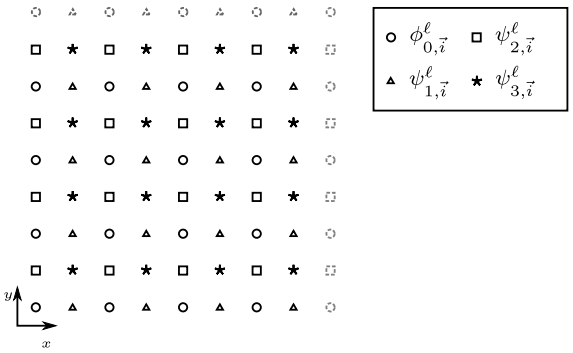

Fig. 2. Part of the first two levels of the dyadic grid indicating the position of the two-dimensional scaling functions and wavelets. Note that the full grid is repeated from the dashed grey points until it contains at least $2m+1$ scaling functions in each direction.

a reduction in computational costs and memory required to construct the reduced internal force vector and tangent stiffness. This procedure was demonstrated on a one-dimensional micro-structure in [20].

2.6. Multi-dimensional wavelet approximation

To obtain the multi-dimensional W-ROM framework, the Deslauriers–Dubuc wavelet basis is employed to approximate all fields in (5) requiring a reduced wavelet integration. The wavelet basis is constructed by scaling and translating a mother scaling function and wavelet ϕ and ψ respectively. In a one-dimensional domain the scaling and translating relations are given by:

$$\phi^{\ell}_{i}(x) = \phi(2^{\ell}x + i) \tag{6a}$$

$$\psi^{\ell}_{i}(x) = \psi(2^{\ell}x + i) \tag{6b}$$

where i and ℓ denote the index and level of the functions. The one-dimensional wavelet basis comprises of a set of scaling functions $\phi^{\ell}_{i}(x) \in \mathcal{S}^{\ell}$ and a set of wavelets $\psi^{\ell}_{i}(x) \in \mathcal{W}^{\ell}$. Each scaling function space is a refinement of its lower level predecessor $\mathcal{S}^{\ell} \subset \mathcal{S}^{\ell+1}$. The union of all the hierarchical approximation spaces spans the complete real space, i.e. $\bigcup_{\ell=0}^{\infty} \mathcal{S}^{\ell} = \mathcal{L}_2(\mathbb{R})$. The wavelet spaces complement the scaling function space such that $\mathcal{S}^{\ell} \oplus \mathcal{W}^{\ell} = \mathcal{S}^{\ell+1}$, enabling a hierarchical decomposition of level $\ell+1$ scaling functions into level ℓ scaling functions and wavelets.

The multi-dimensional wavelet basis, consisting of scaling functions $\phi^{\ell}_{0,\vec{i}}(\vec{x}) \in \mathcal{S}^{\ell}$ and wavelets $\psi^{\ell}_{\lambda,\vec{i}}(\vec{x}) \in \mathcal{W}^{\ell}$, is formed by D outer-products of the one-dimensional scaling functions $\phi^{\ell}_{i}(x)$ and wavelets $\psi^{\ell}_{i}(x)$ respectively. Here, D denotes the dimensionality of the problem. This results in a single scaling function and 2^D-1 wavelet types. The wavelets are labelled with a wavelet type $\lambda = 1, .., 2^D - 1$ to distinguish the different wavelet outer-products. The index of the dyadic grid point corresponding to the scaling function or wavelet is denoted by $\vec{i} = (i_1, i_2, \ldots, i_D)^{\mathrm{T}}$. Note that each index $\vec{i}$ has only a single wavelet type λ assigned to it, i.e. $\lambda = \lambda(\vec{i})$. The following scaling functions and wavelets are present when considering a two-dimensional wavelet basis.

$$\phi^{\ell}_{0,\vec{i}}(\vec{x}) = \phi^{\ell}_{i_1}(x) \otimes \phi^{\ell}_{i_2}(y) \tag{7a}$$

$$\psi^{\ell}_{1,\vec{i}}(\vec{x}) = \psi^{\ell}_{i_1}(x) \otimes \phi^{\ell}_{i_2}(y) \tag{7b}$$

$$\psi^{\ell}_{2,\vec{i}}(\vec{x}) = \phi^{\ell}_{i_1}(x) \otimes \psi^{\ell}_{i_2}(y) \tag{7c}$$

$$\psi^{\ell}_{3,\vec{i}}(\vec{x}) = \psi^{\ell}_{i_1}(x) \otimes \psi^{\ell}_{i_2}(y) \tag{7d}$$

Similar to the one-dimensional W-ROM, the multi-dimensional scaling functions and wavelets are ordered in a dyadic grid. The grid contains at least $2m+1$ initial grid points in each dimension, where m is the degree of the Deslauriers–Dubuc wavelet used, allowing full support of the scaling functions and wavelets. A schematic representation of the location of the two-dimensional scaling function and wavelets in a part of the dyadic wavelet grid is shown in Fig. 2.

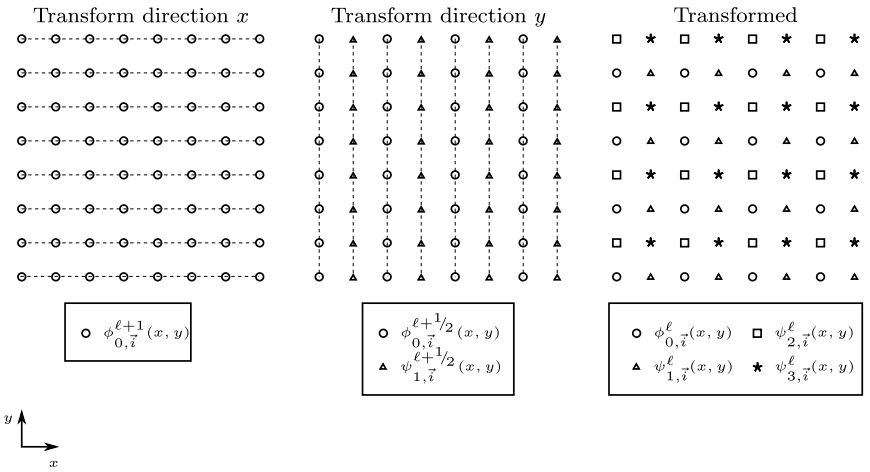

Fig. 3. Scheme of the wavelet transformation of level $\ell+1$ scaling function coefficients to level ℓ scaling function and wavelet coefficients on a two-dimensional dyadic grid using a two-step process.

Functions $f(\vec{x}) \in \mathcal{L}_2(\mathbb{R})$ can be written as a linear combination of scaling functions and (possibly) wavelets using scaling function and wavelet coefficients $s^0_{\vec{i}}$ and $d^{\ell}_{\vec{i}}$ respectively. The function $f(\vec{x})$ can be represented by a basis spanning all scaling functions:

$$f(\vec{x}) = \sum_{\ell} \sum_{\vec{i}} s^{\ell}_{\vec{i}} \phi^{\ell}_{0,\vec{i}}(\vec{x}) \tag{8}$$

using $\lambda = \lambda(\vec{i})$. The scaling function representation can also be hierarchically decomposed into a wavelet representation of function $f(\vec{x})$ after performing a multi-resolution wavelet transform:

$$f(\vec{x}) = \sum_{\vec{i}} s^0_{\vec{i}} \phi^0_{0,\vec{i}}(\vec{x}) + \sum_{\ell} \sum_{\vec{i}} d^{\ell}_{\vec{i}} \psi^{\ell}_{\lambda,\vec{i}}(\vec{x}) \tag{9}$$

To transform the scaling function coefficients on level $\ell+1$ to a set of scaling and wavelet function coefficients on level ℓ, D transformations are required. During the multi-dimensional wavelet transform each direction is transformed subsequently using the one-dimensional wavelet transform. This process is schematically depicted in Fig. 3. By applying this procedure repetitively over the remaining scaling functions, a multi-resolution wavelet transform is obtained.

2.6.1. Adaptive wavelet analysis and synthesis

The *Wavelet Adaptive Multi-resolution Representation* (WAMR) framework by Paolucci et al. [29] is adopted to arrive at a sparse wavelet approximation of the required microstructural fields through an adaptive refinement strategy. This framework comprises of an *Adaptive Fast Wavelet Transform* (AFWT) and the inverse Adaptive Fast Wavelet Transform (AIWT) outlined in the Appendix.

The WAMR is obtained by transforming and recovering the sparsely sampled dyadic grid using the AFWT and its inverse respectively. This allows higher level $\ell+1$ neighbouring grid points to be analysed in wavelet form by sampling the points and transforming them using the AFWT Algorithm. This yields the wavelet discretised field in terms of scaling function coefficients ($\ell = 0$) and wavelet coefficients (for $\ell > 0$). The grid points with a normalised wavelet coefficient $d^{\ell}_{\vec{i}}$ smaller than a predetermined wavelet tolerance δ^{w} are truncated. This leads to a sparse grid representing the *essential points*.

The set of essential points does not necessarily contain all coefficients required to perform the wavelet transform or its inverse, as indicated by Paolucci et al. [29]. The complete set of required scaling function and wavelet coefficients is called the *minimum index set*. To complete the set of essential points, such that all wavelet coefficients used in the transform are present, a set of *non-essential points* (with $d^{\ell}_{\vec{j}} < \delta^{\mathrm{w}}$) is sampled using the MINIDX algorithm (the Appendix, Algorithm 5).

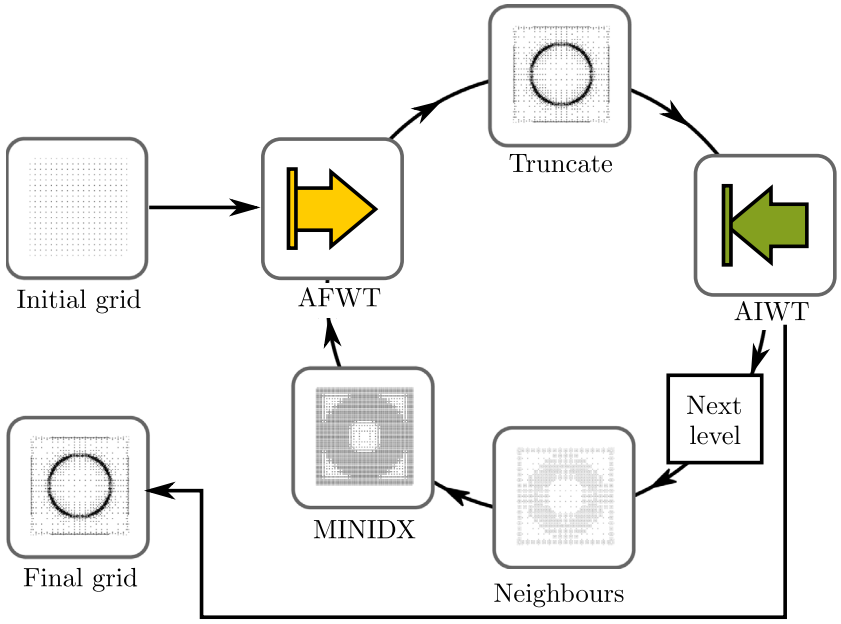

Fig. 4. Schematic representation of the sequence of algorithms to obtain the WAMR.

Table 1
The 4th degree Deslauriers–Dubuc wavelet coefficients.

j	-5	-4	-3	-2	-1	0	1	2	3	4	5
h_j	0	0	$-\frac{1}{16}$	0	$\frac{9}{16}$	1	$\frac{9}{16}$	0	$-\frac{1}{16}$	0	0

This process is repeated until there are no new neighbouring points with normalised wavelet coefficients $d^{\ell}_{\vec{j}} \geq \delta^{\mathrm{w}}$ or when the maximum level L is reached. The multi-resolution analysis of a multi-dimensional field using the sparse wavelet transforms and the MINIDX algorithm is schematically outlined in the flowchart in Fig. 4.

For completeness, the algorithms AFWT and AIWT, as well as MINIDX and the adaptive *Multi-Dimensional Wavelet Approximation* (MDWA), are outlined in the Appendix. The 4th degree Deslauriers–Dubuc wavelet family is used throughout this paper in both the AFWT and AIWT algorithm, for which the filter coefficients are listed in Table 1.

2.7. Micro-structural field approximation by wavelets

The strain fluctuation modes $\underline{\boldsymbol{M}}(\vec{x})$ required to construct the ROM (5) are given by:

$$\underline{\boldsymbol{M}}(\vec{x}) = \vec{\nabla}^{\mathrm{s}} \underline{\vec{R}}(\vec{x}) \tag{10}$$

To store the strain modes on the wavelet grid, each of the modal micro-fluctuation strain components, i.e. M_{xx}, M_{yy} and M_{xy}, is sampled using the MDWA Algorithm. This yields a sparse wavelet representation of each modal strain. Note that the same sparse wavelet grid is used for all modal strain-components.

2.7.1. Interpolation of the microscopic strain and history

To interpolate wavelet data on a single dyadic grid point, the *Hierarchical Adaptive Inverse Wavelet Transform* (HAIWT) is introduced (see Algorithm 1) based on the AIWT Algorithm. The set of indices present in the level ℓ wavelet grid is denoted by $\mathcal{I}^{\ell}$. The set of coordinates belonging to the indices in $\mathcal{I}^{\ell}$ is denoted by $\mathcal{X}^{\ell}$. The set of scaling function coefficients $\mathcal{A}_f$ resulting from the projection of function $f(\vec{x})$ onto the basis of scaling functions

$\bigcup_{\ell=0}^{L} \mathcal{S}^{\ell}$ is given by:

$$\mathcal{A}_f = \bigcup_{\ell=0}^{L} \left\{ s_{\vec{i}}^{\ell} | \, \vec{i} \in \mathcal{I}^{\ell} \right\} \tag{11}$$

where $s_{\vec{i}}^{\ell}$ is the scaling function coefficient at level ℓ and grid point $\vec{i}$. The set of scaling function and wavelet coefficients $\mathcal{B}_f$ projecting the function $f(\vec{x})$ onto the basis of $\mathcal{S}^0 \oplus \bigcup_{\ell=1}^{L} \mathcal{W}^{\ell}$, resulting after the AFWT, is given by:

$$\mathcal{B}_f = \left\{ \left\{ s_{\vec{i}}^{0} | \, \vec{i} \in \mathcal{I}^{0} \right\}, \bigcup_{\ell=1}^{L} \left\{ d_{\vec{i}}^{\ell} | \, \vec{i} \in \mathcal{I}^{\ell} \right\} \right\} \tag{12}$$

where $d_{\vec{i}}^{\ell}$ is the wavelet coefficient at level ℓ and grid point $\vec{i}$.

The microstructural fields, such as the modal strain fluctuations $\underline{\boldsymbol{M}}(\vec{x})$ and history parameters $\underline{\xi}^t$, can be reconstructed using HAIWT. The microstructural strain $\boldsymbol{\varepsilon}(\vec{x}) = \boldsymbol{\varepsilon}_M + \sum_j W_j \boldsymbol{M}_j(\vec{x})$ of the ROM as presented in Eq. (5) is recovered by a summation of the macroscopic strain $\boldsymbol{\varepsilon}_M$ with the reconstructed modal components $\underline{\boldsymbol{M}}(\vec{x})$ weighted with their corresponding modal coefficients $\underline{W}$. The history-parameters are discretised in a similar fashion using the sparse wavelet representation of each parameter field. Note that this may require the interpolation of new dyadic grid points, when local refinement is required to track the microstructural internal force.

Algorithm 1 HAIWT

Require: The wavelet filter coefficients $\underline{h}$, the requested index $\vec{i}$, the scaling function and wavelet coefficients $\mathcal{B}_f$ and the current and maximum level ℓ and L, respectively

if $\ell = 0$ **then**
  return $s_{\vec{i}}^{0}$
end if
$\Delta^{\ell} \leftarrow 2^{L-\ell}$ ▷ Index strides on level ℓ
$\Delta^{\ell-1} \leftarrow 2^{L-\ell+1}$ ▷ Index strides on level $\ell - 1$
for $n \in \{x, y\}$ **do**
  if $\vec{i}$ does not require transform in direction n **then**
    continue
  end if
  $\vec{j} \leftarrow \vec{i}$
  for $k \in [-m/2, m/2 - 1]$ **do**
    $j_n \leftarrow i_n - k\Delta^{\ell-1} - \Delta^{\ell}$ ▷ Find the lower level grid points
    Apply PBC to $\vec{j}$
    $s_{\vec{j}}^{\ell-1} \leftarrow \text{HAIWT}(\mathcal{B}_f, \vec{j}, \ell - 1, L)$ ▷ Transform lower level
    $s_{\vec{i}}^{\ell} \leftarrow s_{\vec{i}}^{\ell} + h_{2k+1} s_{\vec{j}}^{\ell-1}$
  end for
end for
return $s_{\vec{i}}^{\ell}$

2.7.2. Storage of the topology

In conventional FE models, the topology of the microstructure, i.e. the distribution of various phases and voids, is determined by the element topology in a conforming mesh. Individual elements represent a specific material. Voids are not discretised at all. In the non-conforming wavelet representation, the notion of elements has disappeared and an alternative procedure to recover the micro-structural topology. The topology of the microstructural model is stored in a wavelet reduced form by applying the sparse multi-resolution wavelet analysis to the material ID field. The material ID of a wavelet grid point can be recovered using HAIWT (Algorithm 1). The sparsely sampled material IDs for a micro-structure with a single central void in a matrix material are shown in Fig. 5.

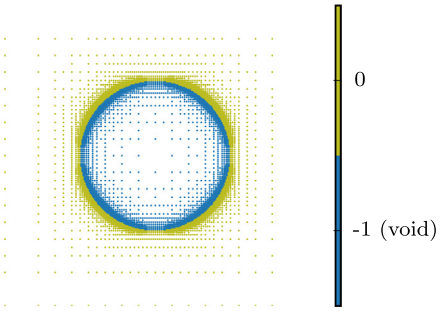

Fig. 5. Example of the sparsely sampled material ID used for the multi-resolution wavelet approximation capturing the topology of a voided matrix.

2.8. Integration of the wavelet approximations

Integration of the wavelet approximated internal force and stiffness integrands yields the reduced internal force and tangent stiffness matrix. The scaling function and wavelet coefficients $s^0_{\vec{i}}$ and $d^\ell_{\vec{i}}$ are constant in space, only the integrals $\int_\mathcal{V} \phi^0_{0,\vec{i}}(\vec{x})\,\mathrm{d}\mathcal{V}$ and $\int_\mathcal{V} \psi^\ell_{\lambda,\vec{i}}(\vec{x})\,\mathrm{d}\mathcal{V}$ are required to solve the integral $\int_\mathcal{V} \tilde{f}(\vec{x})\,\mathrm{d}\mathcal{V}$ of the wavelet discretised field $\tilde{f}(\vec{x})$.

Using Eq. (7) and the orthogonality of the outer-products used to construct the basis, it follows that the two-dimensional integrals can be expanded into products of the one-dimensional integrals:

$$\int_\mathcal{V} \phi^\ell_{0,\vec{i}}(\vec{x})\,\mathrm{d}\mathcal{V} = \int_x \phi^\ell_{i_1}(x)\,\mathrm{d}x \int_y \phi^\ell_{i_2}(y)\,\mathrm{d}y \tag{13a}$$

$$\int_\mathcal{V} \psi^\ell_{1,\vec{i}}(\vec{x})\,\mathrm{d}\mathcal{V} = \int_x \psi^\ell_{i_1}(x)\,\mathrm{d}x \int_y \phi^\ell_{i_2}(y)\,\mathrm{d}y \tag{13b}$$

$$\int_\mathcal{V} \psi^\ell_{2,\vec{i}}(\vec{x})\,\mathrm{d}\mathcal{V} = \int_x \phi^\ell_{i_1}(x)\,\mathrm{d}x \int_y \psi^\ell_{i_2}(y)\,\mathrm{d}y \tag{13c}$$

$$\int_\mathcal{V} \psi^\ell_{3,\vec{i}}(\vec{x})\,\mathrm{d}\mathcal{V} = \int_x \psi^\ell_{i_1}(x)\,\mathrm{d}x \int_y \psi^\ell_{i_2}(y)\,\mathrm{d}y \tag{13d}$$

Hence, the integration procedure for one-dimensional Deslauriers–Dubuc scaling functions and wavelets described in [20] carries over to the multi-dimensional integrals, leading to:

$$\int_\mathcal{V} \phi^\ell_{0,\vec{i}}(\vec{x})\,\mathrm{d}\mathcal{V} = \alpha(\ell)\beta(0)\Delta x_0 \Delta y_0 \tag{14a}$$

$$\int_\mathcal{V} \psi^\ell_{\lambda,\vec{i}}(\vec{x})\,\mathrm{d}\mathcal{V} = \alpha(\ell)\beta(\lambda)\Delta x_0 \Delta y_0 \tag{14b}$$

where Δx_0 and Δy_0 are the dyadic grid spacing in x and y directions on level 0. The factor that scales the integral between different grid levels is given by:

$$\alpha(\ell) = \begin{cases} 1 & \text{if } \ell = 0 \\ 2^{-D(\ell-1)} & \text{if } \ell > 0 \end{cases} \tag{15}$$

The integrals of the coarsest level scaling functions and wavelets are related to the grid size $\Delta x_0 \Delta y_0$ using the following factors:

$$\beta(\lambda) = \begin{cases} 1 \cdot 1 = 1 & \text{if } \lambda = 0 \\ 0.5 \cdot 1 = 0.5 & \text{if } \lambda = 1 \\ 1 \cdot 0.5 = 0.5 & \text{if } \lambda = 2 \\ 0.5 \cdot 0.5 = 0.25 & \text{if } \lambda = 3 \end{cases} \tag{16}$$

derived from relations (13), where the factors originate from the one-dimensional integrals of the Deslauriers–Dubuc scaling function $\int_x \phi^0_i(x)\,\mathrm{d}x = \Delta x_0$ and $\int_x \psi^1_i(x)\,\mathrm{d}x = 0.5\Delta x_0$. The scaling factors $\alpha(\ell)$ are derived from a change of coordinate system, as demonstrated in [20].

The integration of the two-dimensional Deslauriers–Dubuc wavelet approximation results in a summation of the integrals of the scaling function times their coefficients and the integrals of the different wavelet types multiplied with their coefficients. Recall that the type of wavelet $\psi^{\ell}_{\vec{i},\lambda}$ follows directly from the grid point index $\lambda(\vec{i})$.

$$\begin{aligned}\int_{\mathcal{V}} \tilde{f}\,\mathrm{d}\mathcal{V} &= \int_{\mathcal{V}} \sum_{\vec{i}} s^{0}_{\vec{i}}\phi^{0}_{\vec{i}}(\vec{x}) + \sum_{\ell=1}^{L}\sum_{\vec{j}} d^{\ell}_{\lambda,\vec{j}}\psi^{\ell}_{\lambda,\vec{j}}(\vec{x})\,\mathrm{d}\mathcal{V} \\ &= \sum_{\vec{i}} s^{0}_{\vec{i}} \int_{\mathcal{V}} \phi^{0}_{\vec{i}}(\vec{x})\,\mathrm{d}\mathcal{V} + \sum_{\ell=1}^{L}\sum_{\vec{j}} d^{\ell}_{\lambda,\vec{j}} \int_{\mathcal{V}} \psi^{\ell}_{\lambda,\vec{j}}(\vec{x})\,\mathrm{d}\mathcal{V} \\ &= \sum_{\vec{i}} s^{0}_{\vec{i}}\alpha(0)\beta(0)\Delta x_0\Delta y_0 + \sum_{\ell=1}^{L}\sum_{\vec{j}} d^{\ell}_{\lambda,\vec{j}}\alpha(\ell)\beta(\lambda)\Delta x_0\Delta y_0 \end{aligned} \tag{17}$$

2.9. Wavelet-reduced order model

The sparse multi-resolution wavelet approximation outlined in the previous section constitutes the core of the multi-dimensional W-ROM and is applied to represent the fields required to compute the internal force integrands and stiffness matrix integrand on a sparse grid, i.e. the material topology, strain $\boldsymbol{\varepsilon}$ from the micro-fluctuations and macroscopic strain contributions, stress $\boldsymbol{\sigma}$ and history $\underline{\xi}^{t+\Delta t}$. The latter fields are stored as sparse scaling function and wavelet coefficients, denoted by $\mathcal{B}_f$ where f is the wavelet approximated field. Untransformed fields consisting of only scaling function coefficients are denoted by $\mathcal{A}_f$. In the case of vector or tensor fields, each component is discretised with its own coefficients. The sparse storage allows for a computationally efficient transformation, integration and interpolation when the field or its integral is required.

2.9.1. Approximation of the internal force and stiffness

The internal force $\underline{f}^{\mathrm{int}}$ and tangent stiffness matrix $\underline{\underline{K}}$ required to solve the ROM presented in Eq. (5) Section 2.4, can be written as a function of their respective integrands $\underline{\varphi}$ and $\underline{\underline{\kappa}}$:

$$\underline{f}^{\mathrm{int}} = \int_{\mathcal{V}} \underline{\varphi}\,\mathrm{d}\mathcal{V} \tag{18}$$

$$\underline{\underline{K}} = \int_{\mathcal{V}} \underline{\underline{\kappa}}\,\mathrm{d}\mathcal{V} \tag{19}$$

The microstructural internal force integrand φ can be approximated using the wavelet approximated modal strain contributions $\underline{\boldsymbol{M}}(\vec{x})$, the microscopic strain $\boldsymbol{\varepsilon}(\vec{x}) = \boldsymbol{\varepsilon}_M + \sum_i \boldsymbol{M}_i(\vec{x})W_i$ and history $\underline{\xi}(\vec{x})$. This yields a wavelet representation of the components of the internal force integrand $\underline{\varphi}$ and the stiffness integrand $\underline{\underline{\kappa}}$ defined by:

$$\underline{\varphi} = \underline{\boldsymbol{M}}(\vec{x}) : \boldsymbol{\sigma}(\boldsymbol{\varepsilon}, \underline{\xi}) \tag{20}$$

$$\underline{\underline{\kappa}} = \underline{\boldsymbol{M}}(\vec{x}) : {}^{4}\mathbb{C}(\boldsymbol{\varepsilon}, \underline{\xi}) : (\underline{\boldsymbol{M}}(\vec{x}))^{\mathrm{T}} \tag{21}$$

where ${}^{4}\mathbb{C} = \frac{\partial \boldsymbol{\sigma}}{\partial \boldsymbol{\varepsilon}}$ represents the material consistent tangent tensor. Note that this formulation of the stress and stiffness integrands is similar to the FE formulation of the weak-form such that the material models used in the FOM can be applied directly in the W-ROM.

During the wavelet approximation of the internal force integrands $\underline{\varphi}$, the stresses are computed on the dyadic grid. By storing the wavelet coefficients of the sampled stresses, the stress field can be integrated and the macroscopic stress tensor $\boldsymbol{\sigma}_M$ can be reconstructed in the post-processing stage.

The W-ROM algorithm, outlined in Algorithm 2, consists of a Newton–Raphson iterative scheme and a *Multi-Goal Multi-Dimensional Wavelet Approximation* (MG-MDWA) to approximate the strain $\boldsymbol{\varepsilon}$, stress $\boldsymbol{\sigma}$ and history $\underline{\xi}^{t+\Delta t}$ field and integrands of the internal forces $\underline{\varphi}$ and the tangent stiffness matrix $\underline{\underline{\kappa}}$ to solve the force-equilibrium (5). The MG-MDWA algorithm, outlined in Algorithm 3, allows for a sparse sampling of the stress fields resulting in less evaluations of the material model and compressed storage of the history field. Stress, strain and internal force fields showing localisation are locally refined up to the imposed wavelet tolerance δ^{w}. This automatically detects

Algorithm 2 W-ROM

Require: The multi-resolution approximation $\mathcal{B}_{\underline{\boldsymbol{M}}}$ of $\underline{\boldsymbol{M}}(\vec{x})$. The wavelet tolerance δ^{w}, wavelet grid points $\vec{x}_{\vec{i}}$, maximum level L and wavelet coefficients $\underline{h}$:

$\underline{W}^* \leftarrow \underline{W}^k$ ▷ Initial guess modal coefficients
$\underline{\xi}^t \leftarrow \underline{\xi}^{t+\Delta t}$ ▷ Initialise history on t with the $t+\Delta t$ history of the previous increment.
$\underline{\varphi}, \boldsymbol{\varepsilon}, \boldsymbol{\sigma}, \underline{\xi}^{t+\Delta t}, \underline{\underline{\kappa}}, \mathcal{I}^* \leftarrow$ MG-MDWA($\boldsymbol{\varepsilon}_M, \underline{W}, \mathcal{B}_{\underline{\boldsymbol{M}}}$)
$\underline{f}^{\mathrm{ext}} \leftarrow \underline{0}$
$\underline{f}^{\mathrm{int}} \leftarrow \int_{\mathcal{V}} \underline{\varphi}\, \mathrm{d}\mathcal{V}$
while $\|\underline{f}^{\mathrm{ext}} - \underline{f}^{\mathrm{int}}\|_2 / \|\underline{f}^{\mathrm{int}}\|_2 > \delta^{\mathrm{nr}}$ **do**
  for $\vec{i} \in \mathcal{I}^*$ **do** ▷ Loop over the sparse wavelet grid $\mathcal{I}^*$
    Compute $\underline{\varphi}, \boldsymbol{\varepsilon}, \boldsymbol{\sigma}, \underline{\xi}^{t+\Delta t}, \underline{\underline{\kappa}}$ on $\vec{i}$ using $\boldsymbol{\varepsilon}_M, \underline{W}^*, \mathcal{B}_{\underline{\boldsymbol{M}}}$
  end for
  $\underline{f}^{\mathrm{ext}} \leftarrow \underline{0}$
  $\underline{f}^{\mathrm{int}} \leftarrow \int_{\mathcal{V}} \underline{\varphi}\, \mathrm{d}\mathcal{V}$
  $\underline{\underline{K}} \leftarrow \int_{\mathcal{V}} \underline{\underline{\kappa}}\, \mathrm{d}\mathcal{V}$
  Solve for $\underline{\Delta W}$ such that $\underline{\underline{K}}\, \underline{\Delta W} = \underline{f}^{\mathrm{ext}} - \underline{f}^{\mathrm{int}}$
  $\underline{W}^* \leftarrow \underline{W}^* + \underline{\Delta W}$
end while
Approximate $\boldsymbol{\sigma}$ using MDWA (Algorithm 6, Appendix)
$\boldsymbol{\sigma}_M \leftarrow \int_{\mathcal{V}} \boldsymbol{\sigma}\, \mathrm{d}\mathcal{V}$

stress and strain localisation occurring while loading the RVE and prevents oversampling in areas where the fields are relatively smooth. This yields a significant reduction in computational time.

Using the wavelet discretised integrands provided by the MG-MDWA algorithm, the internal force and tangent stiffness are integrated. The Newton–Raphson solution procedure in the W-ROM is then applied to restore the wavelet reduced linear-momentum balance equation.

In this work, the wavelet coefficients are pruned based on the wavelet coefficients of the internal force integrand. The method can be extended in a straightforward manner to support cyclic loading. The history variables generally remain constant. The quality of the history parameter discretisation is then ensured by adding a second criterion for the truncation of wavelet grid points. Only grid points for which the wavelet coefficients of the history parameters are below the set wavelet tolerance may be truncated.

Note that, as the sparse wavelet approximations of both the microstructural stress, strain and history are available, the full-fields are easily recovered using the AIWT algorithm. The macroscopic stress $\boldsymbol{\sigma}_M$ can be directly integrated from the sparse wavelet discretisation of the microstructural stress field. When a more accurate local approximation of the stresses is required, the microstructural stress WAMR can be reconstructed *a-posteriori* according to Eq. (1) up to the wavelet tolerance δ^{w} using the obtained modal fluctuation coefficients $\underline{W}$.

The complete offline and online procedures to construct and run the W-ROM algorithm are schematically outlined in Fig. 6. The offline procedure is performed only once to construct the W-ROM. The steps to evaluate the W-ROM, denoted as the online procedure, are repeated whenever the microstructural model needs to be solved, i.e. in those integration points where the macro-scale model needs to be re-evaluated during the incremental iterative process.

3. Numerical examples

The accuracy and performance of the multi-dimensional W-ROM algorithm is evaluated using two examples. In the first example, a microstructural model with a single central void is considered. In this example, the work flow is demonstrated in detail and the number of dyadic grid points required to perform the integration up to the pre-set tolerance δ^{w} is compared against the number of integration points in the original model to quantify the compression ratio.

The second test-case entails a microstructural model representing a composite material consisting of fibres bonded with a resin. This example demonstrates the effect of the magnitude of the wavelet tolerance on the resulting

Algorithm 3 Multi-Goal MDWA (MG-MGWA)

Require: The fluctuation strain mode scaling function and wavelet coefficients $\mathcal{B}_{\underline{\boldsymbol{M}}}$, the reduced strain micro-fluctuation coefficients $\underline{W}$, the macroscopic strain $\boldsymbol{\varepsilon}_M$, the wavelet tolerance δ^{w} and the wavelet grids $\mathcal{I}^{\ell}$.

$\mathcal{I}^{*} \leftarrow \mathcal{I}^{0} \oplus \mathcal{I}^{1}$ ▷ Define grid
for $\vec{i} \in \mathcal{I}^{*}$ **do** ▷ Sample initial grid points
  $\underline{\xi}_{\vec{i}} \leftarrow \mathrm{HAIWT}(\mathcal{B}_{\underline{\xi}^{t}}, \vec{i}, \ell, L)$
  $\underline{\boldsymbol{M}}_{\vec{i}} \leftarrow \mathrm{HAIWT}(\mathcal{B}_{\underline{\boldsymbol{M}}}, \vec{i}, \ell, L)$
  $\boldsymbol{\varepsilon}_{\vec{i}} \leftarrow \boldsymbol{\varepsilon}_M + \underline{W}^{\mathrm{T}} \underline{\boldsymbol{M}}_{\vec{i}}$
  $\boldsymbol{\sigma}_{\vec{i}},\ {}^{4}\mathbb{C}_{\vec{i}},\ \underline{\xi}^{t+\Delta t}_{\vec{i}} \leftarrow \boldsymbol{\sigma}(\boldsymbol{\varepsilon}_{\vec{i}}, \underline{\xi}_{\vec{i}})$
  $\underline{\varphi}_{\vec{i}} \leftarrow \boldsymbol{M}_{\vec{i}} : \boldsymbol{\sigma}_{\vec{i}}$
  $\underline{\underline{\kappa}}_{\vec{i}} \leftarrow \underline{\boldsymbol{M}}_{\vec{i}} : \boldsymbol{\sigma}_{\vec{i}} : (\underline{\boldsymbol{M}}_{\vec{i}})^{\mathrm{T}}$
  $\underline{s}_{\mathrm{nrm}} \leftarrow \max(\underline{s}_{\mathrm{nrm}}, |\underline{\varphi}_{\vec{i}}|)$ ▷ Normalisation internal force
end for
$\mathcal{B}_{\underline{\varphi}} \leftarrow \mathrm{AFWT}(\mathcal{A}_{\underline{\varphi}})$
for $\ell = 1$ to L **do**
  $\mathcal{I}^{*} \leftarrow \{\vec{i} \,|\underline{d}_{\vec{i}}/\underline{s}_{\mathrm{nrm}} > \delta^{\mathrm{w}}, \underline{d}_{\vec{i}} \in \mathcal{B}_{\underline{\varphi}}\}$ ▷ Truncate
  $\mathcal{N}^{\ell+1} \leftarrow \{\vec{k} \,|\text{where } \vec{k} \text{ is a } \ell+1 \text{ neighbour of } \vec{i} \in \mathcal{I}^{*} \cap \mathcal{I}^{\ell}\}$ ▷ Neighbouring points
  $\mathcal{M}^{*} \leftarrow \mathrm{MINIDX}(\mathcal{N}^{\ell+1} \bigcup \mathcal{I}^{*})$
  $\mathcal{A}_{\underline{\varphi}} \leftarrow \mathrm{AIWT}(\mathcal{B}_{\underline{\varphi}})$
  for $\vec{i} \in \mathcal{M}^{*} \setminus \mathcal{I}^{*}$ **do** ▷ Sample new grid points
    $\underline{\xi}_{\vec{i}} \leftarrow \mathrm{HAIWT}(\mathcal{B}_{\underline{\xi}^{t}}, \vec{i}, \ell, L)$
    $\underline{\boldsymbol{M}}_{\vec{i}} \leftarrow \mathrm{HAIWT}(\mathcal{B}_{\underline{\boldsymbol{M}}}, \vec{i}, \ell, L)$
    $\boldsymbol{\varepsilon}_{\vec{i}} \leftarrow \boldsymbol{\varepsilon}_M + \underline{W}^{\mathrm{T}} \underline{\boldsymbol{M}}_{\vec{i}}$
    $\boldsymbol{\sigma}_{\vec{i}},\ {}^{4}\mathbb{C}_{\vec{i}},\ \underline{\xi}^{t+\Delta t}_{\vec{i}} \leftarrow \boldsymbol{\sigma}(\boldsymbol{\varepsilon}_{\vec{i}}, \underline{\xi}_{\vec{i}})$
    $\underline{\varphi}_{\vec{i}} \leftarrow \boldsymbol{M}_{\vec{i}} : \boldsymbol{\sigma}_{\vec{i}}$
    $\underline{\underline{\kappa}}_{\vec{i}} \leftarrow \underline{\boldsymbol{M}}_{\vec{i}} : \boldsymbol{\sigma}_{\vec{i}} : (\underline{\boldsymbol{M}}_{\vec{i}})^{\mathrm{T}}$
  end for
  $\mathcal{B}_{\underline{\varphi}} \leftarrow \mathrm{AFWT}(\mathcal{A}_{\underline{\varphi}})$
  $\mathcal{I}^{*} \leftarrow \mathcal{I}^{*} \bigcup \mathcal{M}^{*}$
end for
$\mathcal{B}^{\ell+1}_{\underline{\underline{\kappa}}} \leftarrow \mathrm{AFWT}(\mathcal{A}_{\underline{\underline{\kappa}}})$
$\mathcal{B}_{\underline{\xi}^{t+\Delta t}} \leftarrow \mathrm{AFWT}(\mathcal{A}_{\underline{\xi}^{t+\Delta t}})$
$\mathcal{B}_{\boldsymbol{\sigma}} \leftarrow \mathrm{AFWT}(\mathcal{A}_{\boldsymbol{\sigma}})$

compression factor. The reduction in number of material model evaluations using different wavelet tolerances will be investigated. In both examples the macro- and microscopic stresses are evaluated and compared with the FOM solutions to establish the accuracy of the W-ROM.

3.1. Example I: Micro-structure with void

In the first example, a micro-structure consisting of an elasto-plastic material with a single void is considered. The void in the centre of the micro-structure leads to stress concentrations and eventually to a plastic deformation band. The original FE-discretised micro-structure (used in the off-line snapshot stage) is depicted in Fig. 7.

A plane-stress material model with isotropic kinematic hardening is employed. A fictitious material with a Young's modulus $E = 1$ GPa, a Poisson's ratio $\nu = 0.3$, a yield-stress $\sigma_{\mathrm{y}} = 20$ MPa and a kinematic hardening rate $H = 10$ MPa, is used. The constitutive law of the elasto-viscoplastic material is described De Souza Neto et al. [30, p. 148]. The employed fine discretisation is sufficiently smooth to ensure that all discontinuities occurring in the

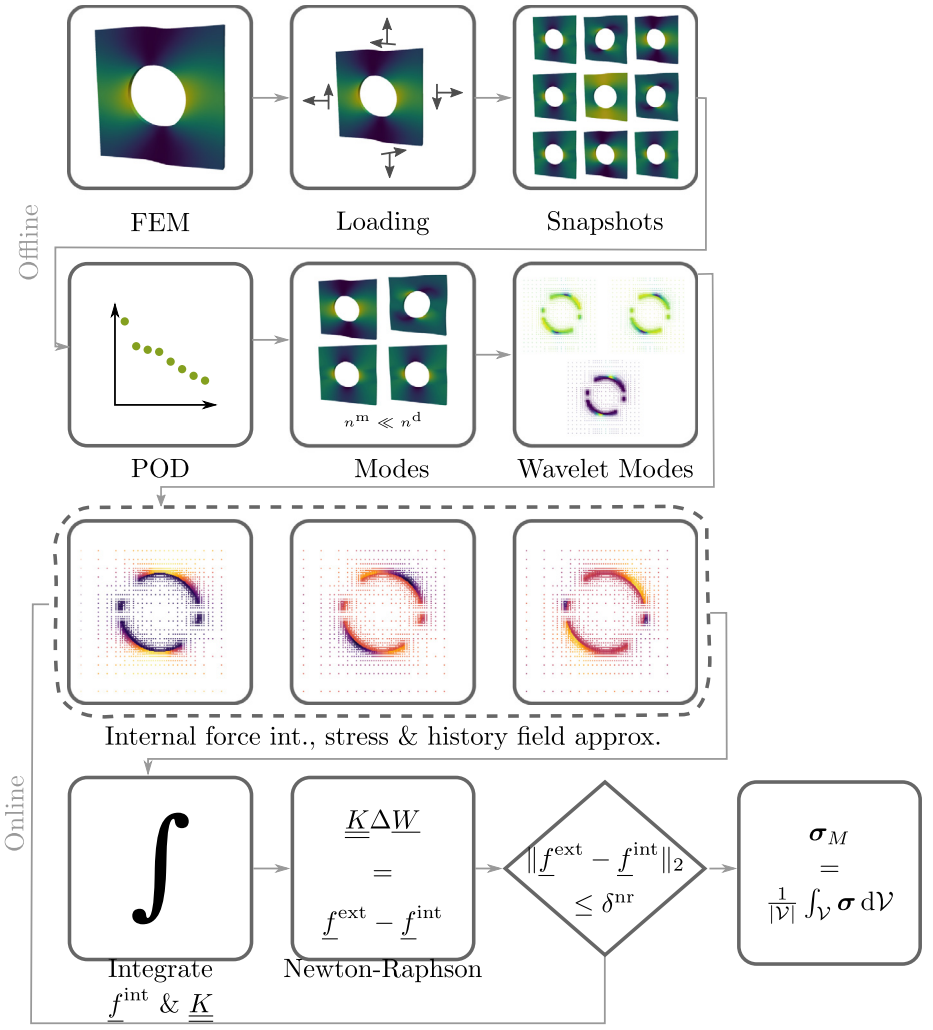

Fig. 6. Schematic representation of the computational steps required to construct the W-ROM offline and exploit it online.

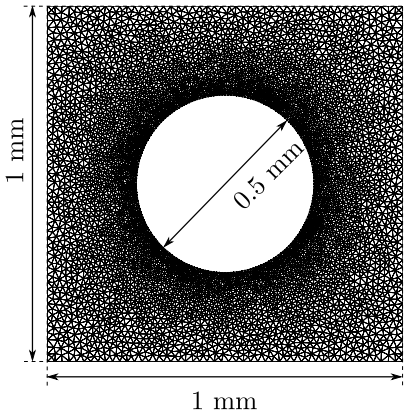

Fig. 7. The finite element discretisation using quadratic Lagrangian triangular elements of the micro-structure with a circular void in the centre.

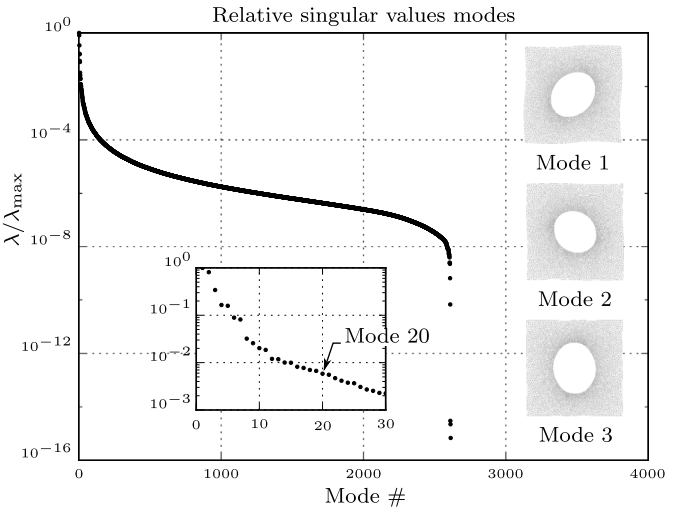

Fig. 8. Example I: The singular values and the first three corresponding modal fluctuation fields obtained from the POD on the snapshots.

strain field at element boundaries are below the imposed wavelet tolerance δ^{w}. Note that, if wavelet tolerances below the magnitude of the discretisation error were to be employed, the W-ROM would approximate the discretisation artefacts of the original model. In other words; the W-ROM can never exceed the accuracy of the FOM used for its construction. As a result, the mesh contains 21 432 nodes and 10 520 elements, which are integrated using a second order Gaussian quadrature leading to 31 560 Gauss points.

3.1.1. Offline stage: snapshots

To accurately sample the kinematics of the microstructural model, the model is loaded using 140 different macroscopic strain directions lying on an ellipsoidal surface spanned by the normalised von Mises strain $\varepsilon_{\mathrm{vm}} = 1$. Of the 140 loading directions, 130 directions are used for the construction of an accurate reduced basis. The 10 remaining directions are used for the verification of the W-ROM. The loading directions are sampled using Latin-Hypercube sampling [31] to cover the entire strain space uniformly. The accurate sampling of the snapshot space allows for the construction of an accurate ROM. In this way, the kinematic contribution of the errors arising from the *reduced basis* are minimised. This enables a fair comparison between the FOM and W-ROM through which the errors arising from the *wavelet reduction* of the integrand can be assessed.

To sample the snapshot space, the micro-structure is loaded up to $\varepsilon_{\mathrm{vm}} = 0.01$ in 30 increments. The micro-fluctuation field of each increment is stored in the snapshot-matrix $\underline{\underline{X}} \in \mathbb{R}^{n^{\mathrm{d}} \times n^{\mathrm{s}}}$, where n^{d} and n^{s} are the number of degrees of freedom (42 864) and snapshots (3900) respectively.

3.1.2. Offline stage: modal approximation kinematics

The POD is applied to the snapshots $\underline{\underline{X}}$ to derive the reduced basis representing FE solutions. The singular values λ and the first three corresponding modal micro-fluctuation fields are plotted in Fig. 8. The first 20 modes are selected to represent the microstructural kinematics.

These 20 FE based micro-fluctuation modes are converted into strain modes and samples as wavelet fields, compressing the sampled snapshots by a factor 195×. A maximum wavelet grid level $L = 5$ is employed, yielding a wavelet grid-spacing of $\sim 3.5 \times 10^{-3}$ mm. The smallest elements (close to the void) have a characteristic length of approximately 8×10^{-3} mm, thereby capturing the original spatial resolution of the FE basis.

A relative wavelet tolerance $\delta^{\mathrm{w}} = 1 \times 10^{-2}$ is employed to allow accurate approximation of the micro-fluctuation strain field discretisation. When a stricter tolerance is desired, the amplitude of the jumps in the strain field can be lowered by employing a finer discretisation or by applying superconvergent patch recovery [32] to prevent the wavelet approximation from picking up the non-physical discontinuities present in the FE discretisation of the strain field. In future work, wavelet-based solutions of the snapshot should be preferred instead. The first three wavelet discretised micro-fluctuation strain modes are shown in Fig. 9.

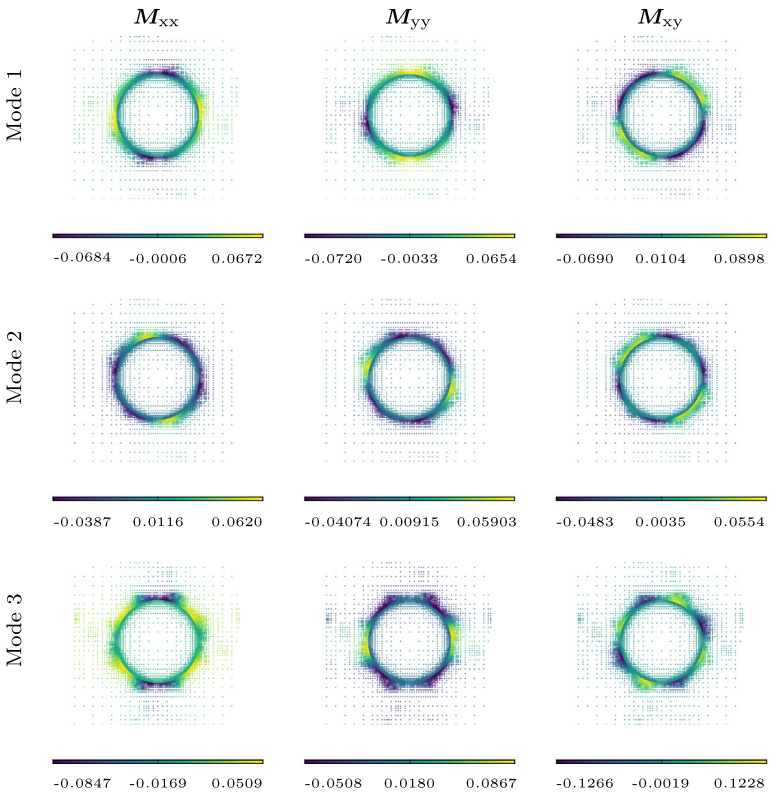

Fig. 9. The wavelet-approximated modal micro-fluctuation strains of the first three modes.

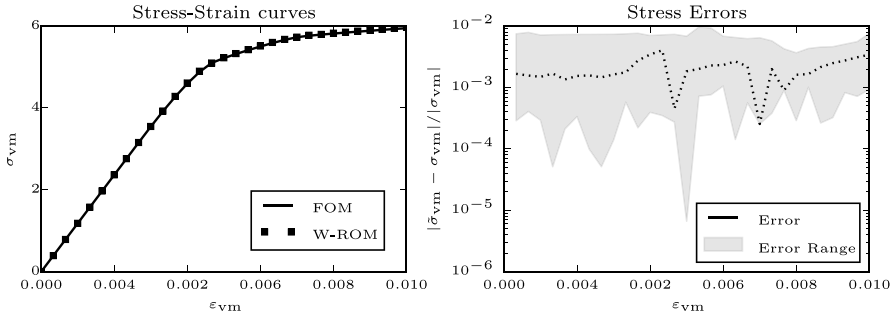

Fig. 10. The macroscopic stress–strain curve for the load case $\boldsymbol{\varepsilon} = [\ 0.0102,\ 0.0170,\ -0.0540]^{\mathrm{T}}$ for the FOM and W-ROM (left) and the corresponding relative error (right). The error range for all 10 load cases is depicted by the light grey region.

3.2. Online stage: macro-scale accuracy

The accuracy of the macroscopic stress approximation of the W-ROM is evaluated for 10 different load-cases. The macroscopic stresses are computed with both FOM and W-ROM. For the W-ROM, a wavelet tolerance of $\delta^{\mathrm{w}} = 1 \times 10^{-1}$ and a maximum level of $L = 5$ are employed. The von Mises stress–strain curve resulting from one of the applied load-cases, $\boldsymbol{\varepsilon} = [0.0102,\ 0.0170,\ -0.0540]^{\mathrm{T}}$ is plotted on the left-hand side of Fig. 10. The relative error in the approximation of the macroscopic stress corresponding to that load-case and the range of relative errors obtained for all 10 load-cases are plotted on the right-hand side.

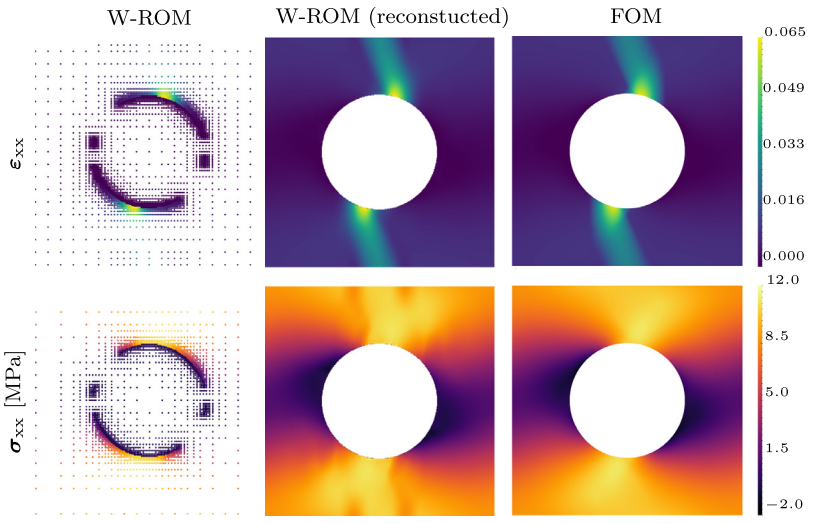

Fig. 11. A comparison of the microstructural ε_{xx} and σ_{xx} components of the strain and stress fields for the final increments (obtained using W-ROM and FOM).

The macroscopic stress–strain curve resulting from the W-ROM model shows an excellent agreement with the stress–strain curve obtained using the FOM. The relative error $\bar{\epsilon}_{\sigma_{\text{vm}}} = |\tilde{\sigma}_{\text{vm}} - \sigma_{\text{vm}}|/|\sigma_{\text{vm}}|$, which includes the error originating from the modal approximation, remains well below the set wavelet tolerance $\delta^{\text{w}} = 10^{-1}$.

3.3. Online stage: micro-scale accuracy

The wavelet approximation of the macroscopic stress resulting from the W-ROM relies on the wavelet approximation of the microstructural stress field. The approximated microstructural stress and strain fields are plotted on the sparse wavelet grid for the final increment of the load-case with $\boldsymbol{\varepsilon} = [0.0118, 0.0160, -0.0184]^{\text{T}}$, see Fig. 11. To assess the accuracy of the W-ROM approximations, the (reconstructed) microstructural stress and strain fields resulting from the FOM and W-ROM model are plotted in Fig. 11 as well. Note that the wavelet reduced model approximates the full stress and strain field by back-transforming the wavelet coefficients using AIWT with zero-valued wavelet coefficients in place of the truncated coefficients. This approach allows for a full reconstruction of all sparsely approximated fields.

As can been seen in Fig. 11, the main features of the deformation and stress fields present in the FOM are recovered by the W-ROM using a wavelet tolerance of $\delta^{\text{w}} = 10^{-1}$.

3.4. Reduction versus accuracy

Table 2 shows the maximum absolute values of the components of the stress and strain fields found by the FOM and W-ROM for the load-case examined above. The values of all components fall within the relative wavelet tolerance of $\delta^{\text{w}} = 10^{-1}$ of their FOM counterpart.

The original FOM made use of 31 560 Gauss quadrature points to integrate the stress and strain fields. The compression factor, i.e. the ratio of wavelet points versus Gauss points in the FOM, for integrating the stress and strain fields in the W-ROM is plotted on the left-hand side of Fig. 12. The number of iterations required to solve the reduced order model is depicted on the right-hand side.

The compression factor in terms of the number of integration points remains relatively constant over the increments. The minor adjustments in the number of integration points are due to rearrangements of the stress field, leading to the addition or deletion of some wavelet grid points.

Table 2
The maximum absolute values of the stress and strain components obtained by FOM and W-ROM, along with the relative errors on each of these components using a wavelet approximation tolerance of $\delta^{\mathrm{w}} = 10^{-1}$.

Model	Dir.	FOM	W-ROM	Error %
$\lvert\varepsilon\rvert_{\max}$	XX	6.19×10^{-2}	6.46×10^{-2}	4.36
	YY	2.58×10^{-2}	2.69×10^{-2}	4.26
	XY	6.61×10^{-2}	6.95×10^{-2}	0.30
$\lvert\sigma\rvert_{\max}$	XX	1.11×10^{1} MPa	1.10×10^{1} MPa	0.90
	YY	5.17×10^{0} MPa	5.25×10^{0} MPa	1.55
	XY	4.92×10^{0} MPa	5.06×10^{0} MPa	2.85

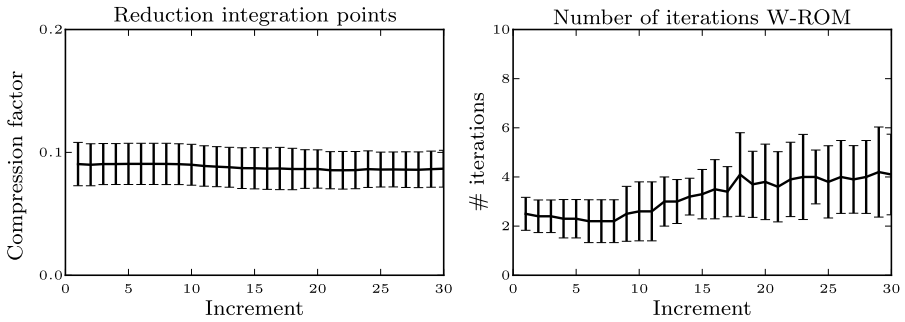

Fig. 12. The average compression factor and its standard deviation of the 10 load cases using $\delta^{\mathrm{w}} = 10^{-1}$ (left) and the average number of iterations, with standard deviation, at each increment for the 10 load-cases (right).

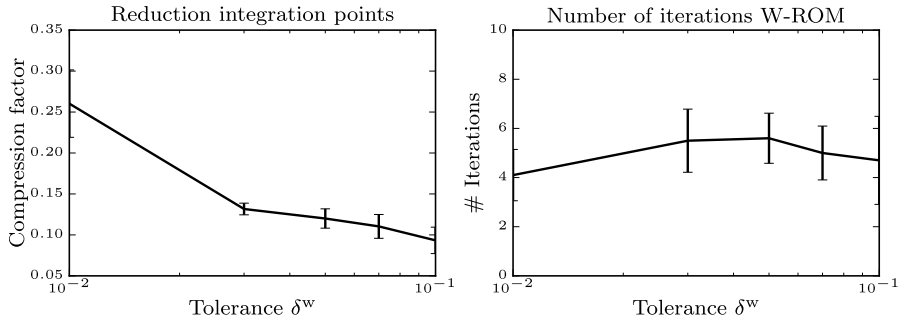

Fig. 13. The average compression factor and its standard deviation for different wavelet approximation tolerances δ^{w} (left). The maximum number of iterations averaged over the 10 load-cases and its standard deviation for different wavelet approximation tolerances δ^{w} (right).

The number of iterations remains relatively constant until increment 10, where the first load-cases start to yield plastic deformation. The plastic deformation leads to more evaluations of the non-linear material model and an increase in the number of iterations. This increase is not larger than what one would expect from FOM, still leading to a decrease in computational time when taking into account the reduction of the required number of integration points.

To identify the effectivity of the reduction, several different wavelet tolerances δ^{w} are used for the W-ROM. The maximum compression factor for each tolerance is shown in Fig. 13. Obviously, the compression factor decreases when the wavelet tolerance δ^{w} on the local approximation is increased. The wavelet tolerance δ^{w} therefore proves to be a suitable instrument to control the approximation accuracy versus the computational cost of a W-ROM model.

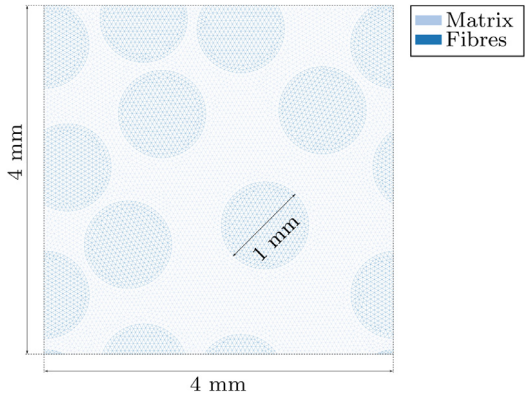

Fig. 14. The finite element discretisation using quadratic Lagrangian triangular elements of the fibre–resin micro-structure. The mesh consists of 31 759 nodes, 15 714 elements which are integrated using a second-order Gaussian quadrature leading to 47 142 Gauss points.

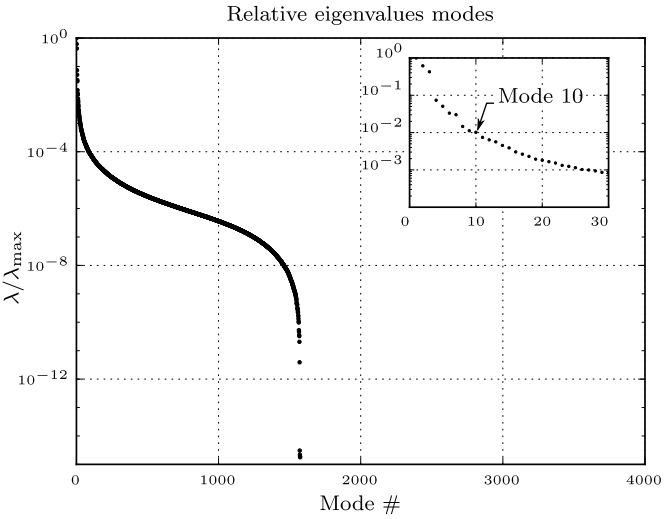

Fig. 15. Example II: The eigenvalues obtained from the POD.

3.5. Example II: Carbon fibre reinforced epoxy

For the second example, a fibre–resin composite is considered. The resin matrix is modelled using an isotropic kinematic hardening material with a Young's modulus $E = 1$ GPa, a Poisson's ratio $\nu = 0.3$ and a yield stress $\sigma_y = 10$ MPa. The hardening modulus is set to $H = 200$ MPa. The fibres are modelled using a linear elastic material with a Young's modulus $E = 1.4$ GPa and a Poisson's ratio of $\nu = 0.3$. The microstructural model is shown in Fig. 14.

3.5.1. Offline stage: modal approximation kinematics

To construct the reduced basis, the snapshots of the microstructural model are collected using the procedure outlined in Example I. Again, a grand total of 3500 snapshots have been collected ensuring accurate sampling of the macroscopic strain space. The resulting normalised singular values are depicted in Fig. 15.

The reduced basis for the strains resulting from the micro-fluctuation field is constructed using the first 10 modes, compressing the sampled snapshots by a factor 350×. The modes are projected on the wavelet approximation using a maximum level of $L = 5$ and a wavelet tolerance of $\delta^w = 10^{-2}$.

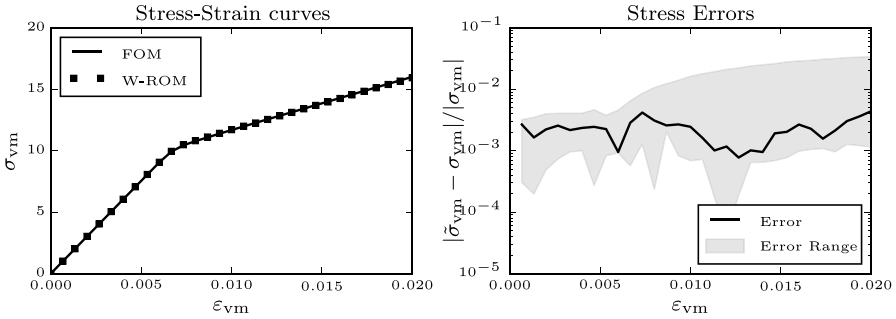

Fig. 16. The stress–strain curve of the RVE for load case LC01 for the FOM versus W-ROM (left) and the relative error (right). The range of relative errors for all 10 load-cases is depicted as the grey region.

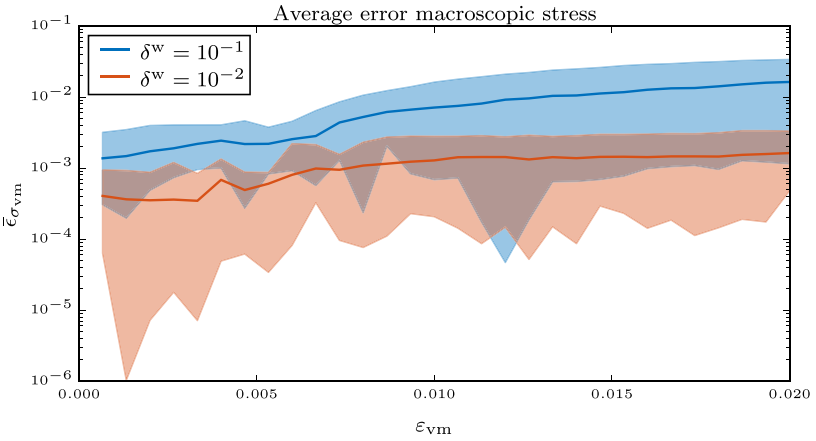

Fig. 17. The average relative errors (line) and spread (shaded area) for the W-ROM approximation of the macroscopic stress with wavelet tolerances $\delta^{\mathrm{w}} = 10^{-1}$ and 10^{-2}.

3.6. Online stage: macro-scale accuracy

To investigate the accuracy of W-ROM with a wavelet tolerance of $\delta^{\mathrm{w}} = 10^{-1}$ in approximating the macroscopic stress, the macro-scale stresses $\boldsymbol{\sigma}_M$ obtained by W-ROM and FOM are compared. The von Mises macroscopic stress–strain curve for the composite micro-structure loaded with a macroscopic strain $\boldsymbol{\varepsilon}_M = [0.0236, -0.0032, -0.0184]^{\mathrm{T}}$ (load-case 1, LC01) is depicted on the left-hand side of Fig. 16. The right-hand side shows the corresponding relative error in the macroscopic stress of LC01 and the band with the relative errors for all 10 load-cases. Note that the range of errors in the macroscopic stresses computed using W-ROM fall well below the relative wavelet tolerance $\delta^{\mathrm{w}} = 10^{-1}$ used for the approximation.

To investigate the influence of the wavelet tolerance δ^{w} on the relative errors in the resulting macroscopic stress, the average error $\bar{\varepsilon}_{\sigma_{\mathrm{vm}}}$ of all 10 load-cases is plotted in Fig. 17 for tolerances $\delta^{\mathrm{w}} = 10^{-1}$ and 10^{-2}. The shaded areas mark the bands with the errors for all 10 load-cases. Again, the errors are controlled by the wavelet tolerance and the accuracy of the homogenised stress σ_M is more accurate then the imposed tolerance δ^{w}.

3.7. Online stage: micro-scale accuracy

To investigate the errors in the microstructural fields, the recovered microstructural stress obtained using the W-ROM with wavelet tolerances $\delta^{\mathrm{w}} = 10^{-1}$ and $\delta^{\mathrm{w}} = 10^{-2}$ are compared to the stress field obtained from the

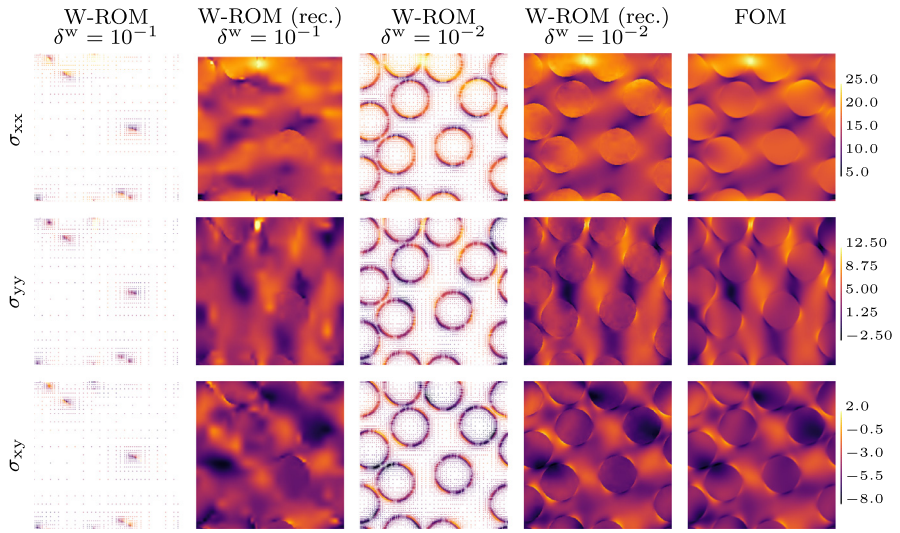

Fig. 18. The microstructural stress fields using FOM and W-ROM with $\delta^w = 10^{-1}$ and 10^{-2}, respectively. The first and third columns show the sparse wavelet fields. The second and fourth columns show the corresponding fully reconstructed fields. The final column shows the FOM result generated using the original FE model.

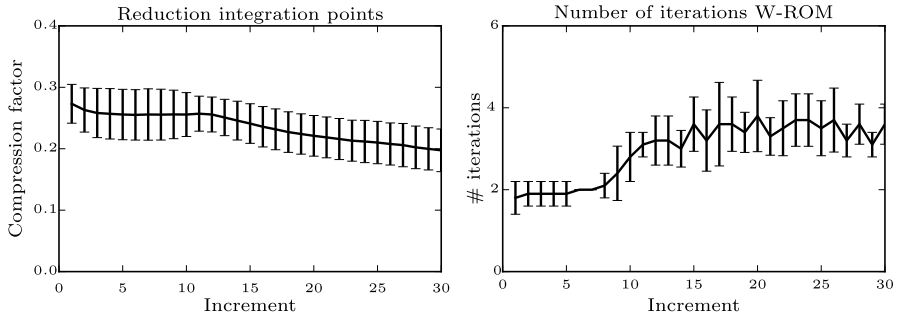

Fig. 19. The reduction of the required integration points W-ROM with $\delta^w = 10^{-1}$. The number of iterations is comparable to the FOM.

FOM. The obtained stress fields are shown in Fig. 18. For the wavelet fields, both the sparse representation and the fully reconstructed fields are plotted.

Both W-ROM approximations capture the same stress bands as found using FOM, which are qualitatively comparable up to the tolerance of the approximation. The W-ROM with a wavelet tolerance of $\delta^w = 10^{-1}$ enables reduction by omitting the approximation of high-frequency components of the stress field, whilst maintaining a good average approximation. If a more detailed reconstruction of the stress field is required, a wavelet approximation with tolerance $\delta^w = 10^{-2}$ is sufficient to recover a sharp plot of the stress field, whilst maintaining a compression factor of $\sim 0.5\times$.

3.8. Reduction

The W-ROM model reduces the 63 518 dofs to only 10 modal coefficients and only 20% to 30% of the number of integration points of the FOM, see Fig. 19.

A significant reduction is obtained with $\delta^w = 10^{-1}$. This wavelet error may seem relatively large, but it defines the local error and is therefore able to recover large features in the microstructural stress and strain fields. This is remarkable, since the highly fluctuating stress field between inclusions is coarsely discretised using sometimes as

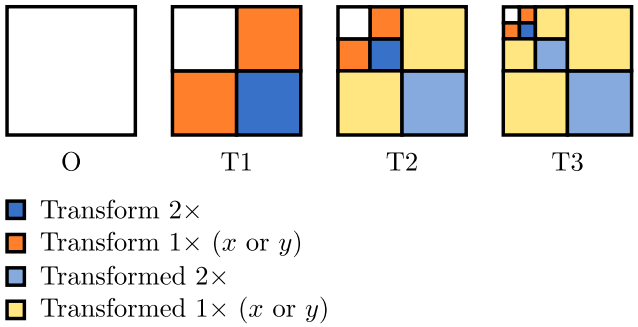

Fig. 20. Schematic representation of the fractions of transformed coefficients in the two-dimensional multi-resolution wavelet transform.

little as 4 elements between fibres, leaving little room for reduction. Only a small number of iterations are needed to converge to the W-ROM solution. Note again, this demonstrates that the error control is a unique feature of the W-ROM methodology.

3.9. Computational costs

The reduction in computational costs in this model arises from the reduction in material point evaluations. In order to select the appropriate subset of material points to evaluate, the wavelet discretisation is adaptive. The applied sparse adaptive wavelet transforms have been developed by Paolucci et al. [29], who showed that adaptive wavelet transforms (i) achieve a great reduction in the number of points to evaluate and (ii) lead to algorithms that are computationally highly efficient.

The current implementation of the wavelet transforms is not yet optimised for speed, making a simple comparison of CPU-times with standard vectorised matrix solvers difficult.

It is however possible to estimate the overhead for the presented examples. Fig. 20 depicts the fraction of transformed coefficients in two dimensions for each step in a three level wavelet transform. The original field is denoted with O and the three transformation steps required to transform all levels are denoted as T1 to T3. For the applied Deslauriers–Dubuc wavelet family the scaling functions remain untransformed (white). The wavelet coefficients require a transform in x, y or both directions. The less saturated fields have been transformed in previous steps.

For a 4th-degree Deslauriers–Dubuc wavelet, 4 *floating point operations* (FLOPs) are required per dimension to transform a scaling coefficient to a wavelet coefficient and vice-versa using the WARM algorithm and its inverse. When the number of coefficients is known, the costs of a fast (inverse) wavelet transform scales as $\mathcal{O}(N) \times 4$ FLOPS, where N is the number of evaluated material points.

The computational overhead of the (sparse) fast wavelet transforms can be compensated through the reduction in number of material model evaluations. Each material point requires the iterative solution of the non-linear material model. The number of FLOPs required for the material model depends on the complexity and the number of iterations required to solve the material model. Let us assume that the number of FLOPs scales with $\mathcal{O}(N) \times \mathcal{O}(I) \times \mathcal{O}(M)$, where I is the number of iterations and M the number of FLOPs required to solve material model for one iteration.

The hierarchical transforms used for the approximation of the history and the material ID should only be performed when new points are required, thereby omitting almost all transforms since the grid is mostly preserved between increments.

The average number of points transformed in the sparse wavelet of the composite up to wavelet level $L = 5$ with tolerance $\delta^{\mathrm{w}} = 10^{-1}$ is approximately 2600 of which $1/3$ is transformed twice (in x and y directions). This yields a total of $(2/3 \times 2600 + 2 \times 1/3 \times 2600) \times 4 \approx 13\,870$ FLOPs per wavelet transform. The W-ROM requires a forward and backward wavelet transform per iteration.

The full-order model in the example uses 47 140 Gauss quadrature points on which the material model needs to be evaluated. Subtracting the number of grid points used for the wavelet discretisation yields a reduction of $47\,140 - 2600 \approx 44\,540$ material model evaluations.

The total reduction of CPU-time depends on the used material model. Therefore a practical example is used to outline the reduction in CPU-time further. When solving a non-linear material model requiring order 10 FLOPs, the following estimate of the reduction in computational time $13\,870/(10 \times 44\,540) \approx 0.03$ is obtained. This estimate does not account for the small overhead resulting from wavelet transforms required for additional points. However an optimised implementation preventing unnecessary forward and backward transforms, ensures that the indicated order of magnitude of the reduction in CPU-times is realistic.

4. Conclusions

This paper presents a novel multi-dimensional hyper-reduced method for microstructural problems arising in computational homogenisation by combining Reduced Order Modelling and wavelet reduction to obtain a compressed linear set of equations. The innovative aspects of this approach are:

- The W-ROM provides an adequate reduction on two-dimensional micro-structures without an *a-priori* determined integration scheme or modal approximation to reduce the computational integration costs.
- The error made in the multi-dimensional approximation of the internal force field is controlled by the imposed wavelet tolerance. This gives the user direct control on the approximation of the internal force balance. When required the wavelets employ an automatic refinement of the local grid. When a less detailed grid is required the method automatically coarsens again.
- The microstructural stress and strain fields are approximated up to the desired wavelet tolerance. The wavelet grid constructed for the internal force integrands are locally enriched to capture stresses in regions without fluctuations in internal forces.
- The macroscopic (averaged) field variables are far more accurate than the (local microstructure) wavelet tolerance imposed.

The method is demonstrated on two periodic structures, one microstructure with a single void in the centre and one microstructure representing a composite micro-structure. The W-ROM algorithm obtains significant compression factors of 10% to 30% of the number of stored history parameters and material models evaluated.

The W-ROM can be extended to three-dimensional problems by constructing a three-dimensional wavelet basis using the outer product between *three* scalar wavelet bases. The adaptation of the sparse wavelet approximations and the integration follows similar procedures as described for the two-dimensional case incorporating all three dimensions.

Furthermore the relation between the required number of sampled points for integration is shown to be inversely proportional to the imposed wavelet tolerance. When stricter tolerances are employed, the W-ROM model starts to approximate the underlying ROM model.

Despite the significant reduction in evaluated integration points, the W-ROM algorithm will still yield a smaller reduction of computational time than Empirical Interpolation Methods or Energy Conserving Sampling and Weighting methods. When minimising the CPU-time alone, the proposed online procedure to obtain the adaptive wavelet grid is simply not present in methods where the evaluated subset of material points is *fixed* during the offline phase. When dealing with *evolving* stress- and strain-fields in the reduced micro-structural models, the adaptivity becomes vital to obtain accurate results.

Acknowledgements

The research leading to these results has received funding from the European Research Council under the European Union's Seventh Framework Programme (FP7/2007-2013)/ERC grant agreement n° [339392].

Appendix. Sparse multi-resolution wavelet algorithms

The discrete forwards multi-dimensional sparse wavelet transform as presented in [29] is shortly outlined in Algorithm 4. The inverse Adaptive Fast Wavelet Transform (AIWT) is obtained by summing from 0 to $L-1$ and switching the subtraction to an addition on line 12.

Algorithm 4 AFWT [29]

Require: The wavelet filter coefficients $\underline{h}$, the scaling function and wavelet coefficients $\mathcal{A}_f$, the wavelet grid $\mathcal{I}^\ell$, the maximum level L.

1: **for** $\ell = L-1$ to 0 **do**
2: $\quad\Delta^\ell \leftarrow 2^{L-\ell}$
3: $\quad\Delta^{\ell+1} \leftarrow 2^{L-\ell-1}$
4: $\quad$**for** $n \in \{x, y\}$ **do**
5: $\quad\quad$**for all** $\vec{i} \in \mathcal{I}^{\ell+1}$ and $\vec{i}$ needs to be transformed in direction n **do**
6: $\quad\quad\quad\vec{j} \leftarrow \vec{i}$
7: $\quad\quad\quad s^{\ell+1}_{\vec{i}} \leftarrow \mathcal{A}_f$
8: $\quad\quad\quad d^{\ell+1}_{\vec{i}} \leftarrow s^{\ell+1}_{\vec{i}}$
9: $\quad\quad\quad$**for** $k \in [-m/2, m/2-1]$ **do**
10: $\quad\quad\quad\quad j_n \leftarrow i_n - k\Delta^\ell - \Delta^{\ell+1}$ ▷ Find the lower level grid points
11: $\quad\quad\quad\quad$Apply PBC to $\vec{j}$ when necessary
12: $\quad\quad\quad\quad s^{\ell}_{\vec{j}} \leftarrow \mathcal{A}_f$
13: $\quad\quad\quad\quad d^{\ell+1}_{\vec{i}} \leftarrow d^{\ell+1}_{\vec{i}} - h_{2k+1} s^{\ell}_{\vec{j}}$
14: $\quad\quad\quad$**end for**
15: $\quad\quad\quad\mathcal{A}_f \leftarrow d^{\ell+1}_{\vec{i}}$ ▷ Swap scaling function and wavelet coef.
16: $\quad\quad$**end for**
17: $\quad$**end for**
18: **end for**

The minimum index set, used to complete the set of essential points such that the sparse scaling function or wavelet discretisation can be transformed, is given in Algorithm 5.

Algorithm 5 MINIDX [29]

Require: Sparse set of essential indices $\mathcal{I}^*$ in the wavelet grid for $\ell = 0, .., L$ and the maximum level L.

1: **for** $\ell = L-1$ to 0 **do**
2: $\quad\Delta^\ell \leftarrow 2^{L-\ell}$
3: $\quad\Delta^{\ell+1} \leftarrow 2^{L-\ell-1}$
4: $\quad$**for** $n \in \{x, y\}$ **do**
5: $\quad\quad$**for all** $\vec{i} \in \mathcal{I}^{\ell+1}$ and $\vec{i}$ needs to be transformed in direction n **do**
6: $\quad\quad\quad\vec{j} \leftarrow \vec{i}$
7: $\quad\quad\quad$**for** $k \in [-m/2, m/2-1]$ **do**
8: $\quad\quad\quad\quad j_n \leftarrow i_n - k\Delta^\ell - \Delta^{\ell+1}$ ▷ Find the lower level grid points
9: $\quad\quad\quad\quad\mathcal{I}^* \leftarrow \mathcal{I}^* \bigcup \{\vec{j}\}$
10: $\quad\quad\quad$**end for**
11: $\quad\quad$**end for**
12: $\quad$**end for**
13: **end for**

The full Multi-Dimensional Wavelet Analysis employed to adaptively up a sparse wavelet discretisation of a field $f(\vec{x})$ is given in Algorithm 6

Algorithm 6 MDWA [29]

Require: The wavelet tolerance δ^{w}, the function $f(\vec{x})$ and the wavelet grids $\mathcal{I}^{\ell}$ and their coordinates $\mathcal{X}^{\ell}$.

$\mathcal{I}^{*} \leftarrow \mathcal{I}^{0} \oplus \mathcal{I}^{1}$ ▷ Define grid

$\mathcal{A}_f^{*} \leftarrow \{f_{\vec{i}}^{\ell} | \vec{i} \ \forall \ \vec{i} \in \mathcal{I}^{*}\}$

$s_{\mathrm{nrm}} \leftarrow \max_{s_{\vec{j}} \in \mathcal{A}_f^{*}}(|s_{\vec{j}}^{\ell}|)$ ▷ Max. scaling function coef.

$\mathcal{B}_f^{*} \leftarrow \mathrm{AFWT}(\mathcal{A}_f^{*})$

for $\ell = 1$ to L **do**

  $\mathcal{I}^{*} \leftarrow \{\vec{i} | \underline{d}_{\vec{i}} / \underline{s}_{\mathrm{nrm}} > \delta^{\mathrm{w}}, \underline{d}_{\vec{i}} \in \mathcal{B}_f\}$ ▷ Truncate

  $\mathcal{N}^{\ell+1} \leftarrow \{\vec{k} | \text{where } \vec{k} \text{ is a } \ell+1 \text{ neighbour of } \vec{i} \in \mathcal{I}^{*} \cap \mathcal{I}^{\ell}\}$ ▷ Neighbouring points

  $\mathcal{M}^{*} \leftarrow \mathrm{MINIDX}(\mathcal{N}^{\ell+1} \bigcup \mathcal{I}^{*})$

  $\mathcal{A}_f^{*} \leftarrow \mathrm{AIWT}(\mathcal{B}_f^{*})$

  $\mathcal{A}_f^{*} \leftarrow \mathcal{A}_f^{*} \oplus \{f_{\vec{i}}^{\ell} | \vec{i} \in \mathcal{M}^{*} \setminus \mathcal{I}^{*}\}$ ▷ Sample new grid points

  $\mathcal{B}_f^{*} \leftarrow \mathrm{AFWT}(\mathcal{A}_f^{*})$

  $\mathcal{I}^{*} \leftarrow \mathcal{I}^{*} \bigcup \mathcal{M}^{*}$

end for

References

[1] M. Geers, V. Kouznetsova, W. Brekelmans, Multi-scale computational homogenization: Trends and challenges, J. Comput. Appl. Math. 234 (7) (2010) 2175–2182, URL http://dx.doi.org/10.1016/j.cam.2009.08.077.

[2] F. Feyel, J.-L. Chaboche, Fe2 multiscale approach for modelling the elastoviscoplastic behaviour of long fibre SiC/Ti composite materials, Comput. Methods Appl. Mech. Engrg. 183 (3–4) (2000) 309–330, URL http://dx.doi.org/10.1016/S0045-7825(99)00224-8.

[3] R. van Tuijl, J. Remmers, M. Geers, Integration efficiency for model reduction in micro-mechanical analyses, Comput. Mech. 62 (2) (2018) 151–169, URL http://dx.doi.org/10.1007/s00466-017-1490-4.

[4] J. Yvonnet, Q.-C. He, The reduced model multiscale method (R3M) for the non-linear homogenization of hyperelastic media at finite strains, J. Comput. Phys. 223 (1) (2007) 341–368, URL http://dx.doi.org/10.1016/j.jcp.2006.09.019.

[5] M. Rathinam, L. Petzold, A new look at proper orthogonal decomposition, SIAM J. Numer. Anal. 41 (5) (2003) 1893–1925, URL http://dx.doi.org/10.1137/s0036142901389049.

[6] D. Ryckelynck, Hyper-reduction of mechanical models involving internal variables, Internat. J. Numer. Methods Engrg. 77 (1) (2009) 75–89, URL http://dx.doi.org/10.1002/nme.2406.

[7] M. Barrault, Y. Maday, N. Nguyen, A. Patera, An 'empirical interpolation' method: application to efficient reduced-basis discretization of partial differential equations, C. R. Math. 339 (9) (2004) 667–672, URL http://dx.doi.org/10.1016/j.crma.2004.08.006.

[8] J. Hernández, J. Oliver, A. Huespe, M. Caicedo, J. Cante, High-performance model reduction techniques in computational multiscale homogenization, Comput. Methods Appl. Mech. Engrg. 276 (2014) 149–189, URL http://dx.doi.org/10.1016/j.cma.2014.03.011.

[9] S. Chaturantabut, D. Sorensen, Nonlinear model reduction via discrete empirical interpolation, SIAM J. Sci. Comput. 32 (5) (2010) 2737–2764, URL http://dx.doi.org/10.1137/090766498.

[10] P. Astrid, S. Weiland, K. Willcox, T. Backx, Missing point estimation in models described by proper orthogonal decomposition, IEEE Trans. Automat. Control 53 (10) (2008) 2237–2251, URL http://dx.doi.org/10.1109/TAC.2008.2006102.

[11] S. An, T. Kim, D. James, Optimizing Cubature for efficient integration of subspace deformations, ACM Trans. Graph. 27 (5) (2008) 165:1–165:10, URL http://dx.doi.org/10.1145/1409060.1409118.

[12] J. Hernández, M. Caicedo, A. Ferrer, Dimensional hyper-reduction of nonlinear finite element models via empirical cubature, Comput. Methods Appl. Mech. Engrg. 313 (2017) 687–722, URL http://dx.doi.org/10.1016/j.cma.2016.10.022.

[13] C. Farhat, T. Chapman, P. Avery, Structure-preserving, stability, and accuracy properties of the energy-conserving sampling and weighting method for the hyper reduction of nonlinear finite element dynamic models, Int. J. Numer. Methods Eng. 102 (5) (2015) 1077–1110, URL http://dx.doi.org/10.1002/nme.4820.

[14] G. Dvorak, Y. Benveniste, On transformation strains and uniform fields in multiphase elastic media, Proc. R. Soc. A 437 (1900) (1992) 291–310, URL http://dx.doi.org/10.1098/rspa.1992.0062.

[15] J. Michel, P. Suquet, Nonuniform transformation field analysis, Int. J. Solids Struct. 40 (25) (2003) 6937–6955, URL http://dx.doi.org/10.1016/S0020-7683(03)00346-9.

[16] S. Roussette, J. Michel, P. Suquet, Nonuniform transformation field analysis of elastic–viscoplastic composites, Compos. Sci. Technol. 69 (1) (2009) 22–27, URL http://dx.doi.org/10.1016/j.compscitech.2007.10.032.

[17] F. Fritzen, M. Leuschner, Reduced basis hybrid computational homogenization based on a mixed incremental formulation, Comput. Methods Appl. Mech. Engrg. 260 (2013) 143–154, URL http://dx.doi.org/10.1016/j.cma.2013.03.007.

[18] I. Daubechies, Ten Lectures on Wavelets, Society for Industrial and Applied Mathematics, 1992, URL http://dx.doi.org/10.1137/1.9781611970104.
[19] C. Harnish, K. Matous, D. Livescu, Adaptive wavelet algorithm for solving nonlinear initial-boundary value problems with error control, Int. J. Multiscale Comput. Eng. 16 (1) (2018) 19–43, URL http://dx.doi.org/10.1615/IntJMultCompEng.2018024915.
[20] R. van Tuijl, C. Harnish, K. Matouš, J. Remmers, M. Geers, Wavelet based reduced order models for microstructural analyses, Comput. Mech. 63 (3) (2019) 535–554, URL http://dx.doi.org/10.1007/s00466-018-1608-3.
[21] M. Brewster, G. Beylkin, A multiresolution strategy for numerical homogenization, Appl. Comput. Harmon. Anal. 2 (4) (1995) 327–349, URL http://dx.doi.org/10.1006/acha.1995.1024.
[22] U. Andersson, B. Engquist, G. Ledfelt, O. Runborg, A contribution to wavelet-based subgrid modeling, Appl. Comput. Harmon. Anal. 7 (2) (1999) 151–164, URL http://dx.doi.org/10.1006/acha.1999.0264.
[23] M. Dorobantu, B. Engquist, Wavelet-based numerical homogenization, SIAM J. Numer. Anal. 35 (2) (1998) 540–559, URL http://dx.doi.org/10.1137/S0036142996298880.
[24] A. Chertock, D. Levy, On wavelet-based numerical homogenization, Multiscale Model. Simul. 3 (1) (2004) 65–88, URL http://dx.doi.org/10.1137/030600783.
[25] H. Flórez, M. Argáez, A model-order reduction method based on wavelets and POD to solve nonlinear transient and steady-state continuation problems, Appl. Math. Model. 53 (2018) 12–31, URL http://dx.doi.org/10.1016/j.apm.2017.08.012.
[26] S. Goedecker, Wavelets and their Application for the Solution of Partial Differential Equations in Physics, Presses polytechniques et universitaires romandes, 1998, URL http://ppur.epfl.ch/livres/2-88074-398-2.html.
[27] R. Hill, Elastic properties of reinforced solids: Some theoretical principles, J. Mech. Phys. Solids 11 (5) (1963) 357–372, URL http://dx.doi.org/10.1016/0022-5096(63)90036-X.
[28] D. Soldner, B. Brands, R. Zabihyan, P. Steinmann, J. Mergheim, A numerical study of different projection-based model reduction techniques applied to computational homogenisation, Comput. Mech. 60 (4) (2017) 613–625, URL http://dx.doi.org/10.1007/s00466-017-1428-x.
[29] S. Paolucci, Z. Zikoski, D. Wirasaet, WAMR: An adaptive wavelet method for the simulation of compressible reacting flow. part I. Accuracy and efficiency of algorithm, J. Comput. Phys. 272 (2014) 814–841, URL http://dx.doi.org/10.1016/j.jcp.2014.01.025.
[30] Eduardo de Souza Neto, D. Peric, D. Owens, Computational Methods for Plasticity : Theory and Applications, John Wiley & Sons, Ltd, 2008, URL http://dx.doi.org/10.1002/9780470694626.
[31] M. Stein, Large sample properties of simulations using latin hypercube sampling, Technometrics 29 (2) (1987) 143–151, URL http://dx.doi.org/10.1080/00401706.1987.10488205.
[32] O. Zienkiewicz, J. Zhu, The superconvergent patch recovery and a posteriori error estimates. Part 1: The recovery technique, Internat. J. Numer. Methods Engrg. 33 (7) (1992) 1331–1364, URL http://dx.doi.org/10.1002/nme.1620330702 arXiv:nme.1620330702.